The Astrophysical Journal, 983:95 (22pp), 2025 April 20 https://doi.org/10.3847/1538-4357/adbe67

oMEGACat. VI. Analysis of the Overall Kinematics of Omega Centauri in 3D: Velocity Dispersion, Kinematic Distance, Anisotropy, and Energy Equipartition

Maximilian Häberle[1], N. Neumayer[1], C. Clontz[1,2], A. C. Seth[2], P. J. Smith[1], S. Kamann[3], R. Pechetti[3], M. S. Nitschai[1], M. Alfaro-Cuello[4], H. Baumgardt[5], A. Bellini[6], A. Feldmeier-Krause[7], N. Kacharov[8], M. Libralato[9], A. P. Milone[10], S. O. Souza[1], G. van de Ven[7], and Z. Wang (王梓先)[2]
[1] Max Planck Institute for Astronomy, Königstuhl 17, D-69117 Heidelberg, Germany; haeberle@mpia.de
[2] Department of Physics and Astronomy, University of Utah, Salt Lake City, UT 84112, USA
[3] Astrophysics Research Institute, Liverpool John Moores University, 146 Brownlow Hill, Liverpool L3 5RF, UK
[4] Centro de Investigación en Ciencias del Espacio y Física Teórica, Universidad Central de Chile, La Serena 1710164, Chile
[5] School of Mathematics and Physics, The University of Queensland, St. Lucia, 4072, QLD, Australia
[6] Space Telescope Science Institute, 3700 San Martin Drive, Baltimore, MD 21218, USA
[7] Department of Astrophysics, University of Vienna, Türkenschanzstrasse 17, 1180 Wien, Austria
[8] Leibniz Institute for Astrophysics, An der Sternwarte 16, 14482 Potsdam, Germany
[9] INAF, Osservatorio Astronomico di Padova, Vicolo dell'Osservatorio 5, Padova, I-35122, Italy
[10] Dipartimento di Fisica e Astronomia "Galileo Galilei," Univ. di Padova, Vicolo dell'Osservatorio 3, Padova, I-35122, Italy

Received 2025 January 16; revised 2025 March 4; accepted 2025 March 5; published 2025 April 10

Abstract

Omega Centauri (ω Cen) is the Milky Way's most massive globular cluster and is likely the stripped nucleus of an accreted dwarf galaxy. In this paper, we analyze ω Cen's kinematics using data from oMEGACat, a comprehensive catalog of ω Cen's central regions, including 1.4 million proper motion measurements and 300,000 spectroscopic radial velocities. Our velocity dispersion profiles and kinematic maps are consistent with previous work but improve on their resolution, precision, and spatial coverage. The cluster's 3D dispersion is isotropic in the core, with increasing radial anisotropy at larger radii. The 2D kinematic maps show an elongation of the velocity dispersion field comparable to the flattening observed photometrically. We find good agreement between proper motions and line-of-sight velocity dispersion, and we measure a kinematic distance of 5494 ± 61 pc, the most precise kinematic distance to ω Cen available. The subset of data with precise metallicity measurements shows no correlation between metallicity and kinematics, supporting the picture of well-mixed stellar populations within the half-light radius of ω Cen. Finally, we study the degree of energy equipartition using a large range of stellar masses. We find partial energy equipartition in the center that decreases towards large radii. The spatial dependence of the radial energy equipartition is stronger than the tangential energy equipartition. Our kinematic observations can serve as a new reference for future dynamical modeling efforts that will help to further disentangle the complex mass distribution within ω Cen.

Unified Astronomy Thesaurus concepts: Globular star clusters (656); Galaxy nuclei (609); Astrometry (80); Proper motions (1295); Radial velocity (1332); Stellar kinematics (1608)

1. Introduction

1.1. Introducing Omega Centauri

Omega Centauri (ω Cen, NGC 5139) is the most massive ($M \approx 3.55 \times 10^6\ M_\odot$; H. Baumgardt & M. Hilker 2018) globular cluster of our Milky Way. The stellar populations within ω Cen are complex and include an unusually wide spread in age (M. Hilker et al. 2004; S. Villanova et al. 2007; S.-J. Joo & Y.-W. Lee 2013; S. Villanova et al. 2014; M. Tailo et al. 2016; C. Clontz et al. 2024a) and metallicity (K. C. Freeman & A. W. Rodgers 1975; C. I. Johnson & C. A. Pilachowski 2010; A. F. Marino et al. 2011; M. S. Nitschai et al. 2024). These complexities are also apparent in the color–magnitude diagram, which shows a multitude of different splits and sequences (A. J. Anderson 1997; E. Pancino et al. 2000; L. R. Bedin et al. 2004; F. R. Ferraro et al. 2004; A. Bellini et al. 2010, 2017b; A. P. Milone et al. 2017; C. Clontz et al. 2024b). For these reasons, ω Cen is now widely accepted to be the stripped nucleus of a dwarf galaxy that has been accreted and disrupted by the Milky Way (e.g., Y. W. Lee et al. 1999; K. Bekki & K. C. Freeman 2003). Other evidence for this accretion scenario has been found by associating ω Cen with stellar streams in the Milky Way Halo (S. R. Majewski et al. 2012; R. A. Ibata et al. 2019) and by finding potential connections with either the Sequoia or the Gaia-Enceladus merger events (D. Massari et al. 2019; G. C. Myeong et al. 2019; D. A. Forbes 2020; J. Pfeffer et al. 2021; G. Limberg et al. 2022; G. Pagnini et al. 2025).

This makes ω Cen the closest nuclear star cluster and an important witness to the formation history of the Milky Way.

Besides its peculiar stellar populations and its likely accreted origin, the internal kinematics of ω Cen have also intrigued astronomers for many years as a way to understand its mass distribution and its formation history. Traditionally, the stellar motions in ω Cen have been studied using line-of-sight velocities, limiting the observable sample to a relatively small number of a few hundred bright, evolved stars (N. B. Suntzeff & R. P. Kraft 1996; M. Mayor et al. 1997; R. A. Reijns et al. 2006). Early ground-based proper-motion studies (F. van Leeuwen et al. 2000) were similarly limited to bright stars, although thousands of individual proper motions could already be measured.

The number of stars for which kinematic measurements are available has changed dramatically with the availability of multi-epoch Hubble Space Telescope (HST) data that has enabled the measurement of proper motions for hundreds of thousands of stars (J. Anderson & R. P. van der Marel 2010; A. Bellini et al. 2014, 2018) down to very faint main-sequence stars. More recently, the MUSE integral field spectrograph (R. Bacon et al. 2010) at the ESO Very Large Telescope has been used to obtain spectra for hundreds of thousands of stars (S. Kamann et al. 2018; M. S. Nitschai et al. 2023; R. Pechetti et al. 2024).

Previous kinematic studies of ω Cen have focused on various aspects of its kinematics including its velocity dispersion (L. L. Watkins et al. 2015a), kinematic distance (G. van de Ven et al. 2006; L. L. Watkins et al. 2015b; H. Baumgardt & E. Vasiliev 2021), rotation (G. Meylan & M. Mayor 1986; D. Merritt et al. 1997; S. Kamann et al. 2018; M. Häberle et al. 2024a; R. Pechetti et al. 2024), and the energy equipartition both in the center (L. L. Watkins et al. 2022) and at larger radii (A. Bellini et al. 2018). These studies showed that ω Cen is rotating with relatively high $\frac{v}{\sigma}$, leading to significant flattening. In addition, the stellar motions show partial energy equipartition and increasing radial anisotropy at larger radii.

The kinematic measurements have also served as the basis for various dynamical modeling efforts using numerous techniques to constrain the mass distribution in ω Cen, which has proved to be a very complex and sometimes inconclusive task. Based on modeling of the inner region, there has been a long debate about the presence of a central, intermediate-mass black hole (E. Noyola et al. 2008, 2010; J. Anderson & R. P. van der Marel 2010; R. P. van der Marel & J. Anderson 2010; A. Zocchi et al. 2017, 2019; H. Baumgardt et al. 2019; A. Bañares-Hernández et al. 2025). The recent discovery of several high proper motion stars near ω Cen's center (M. Häberle et al. 2024b) provided the latest piece in this puzzle and was used to estimate a lower limit for the mass of an intermediate-mass black hole of $M_{\mathrm{IMBH}} > 8200\,M_{\odot}$.

1.2. The oMEGACat Project

In the oMEGACat project, we have created the most comprehensive spectroscopic and astro-photometric data set for ω Cen to date. The basis for this project is two large data sets that cover the half-light radius ($r_{\mathrm{HL}} = 287''$; H. Baumgardt & M. Hilker 2018) of ω Cen: first, an extensive mosaic with VLT MUSE integral field observations. Based on these observations, M. S. Nitschai et al. (2023), hereafter Paper I, provided a spectroscopic catalog with metallicities and line-of-sight (LOS) velocities for over 300,000 stars within the half-light radius of ω Cen. The second component of the project is a large astrometric and photometric catalog (see M. Häberle et al. 2024a, hereafter Paper II), which includes high-precision proper motions and multiband photometry for around 1.4 million sources based on hundreds of new and archival HST observations.

The combined data set enables a broad range of science cases, including studies of the metallicity distribution of various subpopulations (M. S. Nitschai et al. 2024), the age–metallicity relation (C. Clontz et al. 2024a), and the abundances of helium (C. Clontz et al. 2024b) and other individual elements.

1.3. This Work: Overall Kinematics of ω Cen in 3D

In this work, we revisit several of the key kinematic properties of ω Cen using the new combined oMEGACat catalogs, significantly extending the spatial coverage, precision, and depth of existing kinematic studies. We describe the data selection in Section 2. Section 3 describes the determination of velocity dispersion, anisotropy, and rotation profiles using all three velocity dimensions and the derivation of a new kinematic distance estimate. Section 4 describes the creation of two-dimensional kinematic maps. In Section 5, we search for potential variations of the kinematics with metallicity, and in Section 6, we provide new detailed measurements of the state of energy equipartition. Finally, Section 7 contains a summary and conclusions.

Our paper stops short of studying the kinematic differences between different subpopulations and fitting dynamical models, both of which will be the content of future work. We make all products of this analysis available in electronic form to facilitate future modeling efforts. The data products released with this paper are described in Appendix A.

2. Data and Quality Selections

The spectroscopic catalog and its creation are described in detail in Paper I; the HST-based astro-photometric catalog is described in Paper II. Here, we only give a brief overview of the catalog content and describe the various quality selections used to restrict the data set to a reliable subsample of cluster member stars.

The spectroscopic catalog is based on observations with the VLT MUSE integral field spectrograph (R. Bacon et al. 2010) with a total of 103 pointings. The observations were obtained for "The MUSE Survey of Galactic Globular Clusters" (PIs: S. Dreizler and S. Kamann; see also S. Kamann et al. 2018) and for GO Program 105.20CG.001 (PI: N. Neumayer). Both data sets were partially observed with and without adaptive optics mode.

The astro-photometric catalog is based on around 800 individual exposures taken with the two HST instruments ACS/WFC and WFC3/UVIS and in various different filters. The data were taken from the Archive or the dedicated Program GO-16777 (PI: A. Seth). The complete underlying data set has been collected and made available via the MAST archive.[11]

We photometrically reduced the data using the KS2 software (see, e.g., A. Bellini et al. 2017a) and measured relative proper motions using the technique introduced in A. Bellini et al. (2014). The typical temporal baseline of the proper-motion measurements is around 20.6 yr, leading to high proper-motion precision. The final catalog contains 1,395,781 sources with a proper-motion measurement. On the faint end, the catalog reaches $m_{\mathrm{F625W}} \approx 25$, while stars brighter than $m_{\mathrm{F625W}} < 13.9$ are typically saturated.

2.1. Selections within the HST Catalog

2.1.1. Astrometric and Photometric Quality Selections

When studying the velocity dispersion, it is important to restrict the data to measurements with reliable proper motions and errors. This is especially true for energy equipartition studies, where a large range of stellar masses—and therefore magnitudes—must be probed. In this study, we use the

---

[11] DOI:10.17909/26qj-g090.

corrected proper motions from Paper II. These proper motions have been corrected for residual spatial and magnitude-dependent effects; the assumed proper-motion errors are the quadratic sum of the errors of the linear proper-motion fit (determined using the actual residuals) and the statistical error on the empirical correction.

We start the selection process with several global cuts on some properties of the astrometric measurements. For all stars, we require the following conditions to be met (see also Figure 18, Appendix, for histograms of these selections):

1. Temporal baseline longer than 10 yr.
2. $N_{\mathrm{used}}/N_{\mathrm{found}}$ fraction > 0.75 This parameter gives the ratio of data points that were used for the proper-motion fit with respect to the total number of available measurements. A low value indicates that many data points were removed during the clipping stage, indicating unreliable astrometry.
3. Reduced $\chi^2 < 5$ for the proper motions fits in both components.

In addition to these astrometric criteria, we require reliable photometry in the two reddest broadband filters in the data set: ACS/WFC F625W and WFC3/UVIS F814W. The reason for these photometric quality cuts is twofold: First, reliable photometry is needed to assess the cluster membership using color–magnitude diagrams and to estimate the mass of individual stars via isochrone fitting. Second, accurate photometry also indicates good astrometric quality, and by using two filters for which the typical time baseline is long (F625W: 2002, F814W: 2022), we can ensure that the astrometric measurements are of good quality throughout the whole monitored temporal baseline, leading to reliable proper motions.

Our photometric selections are similar to the exemplary ones described in Paper II and provided in the catalog, but slightly stricter. For both filters (F625W, F814W) we require:

1. No saturation (this leads to the exclusion of all red-giant-branch stars with $m_{\mathrm{F625W}} < 13.8$).
2. A quality-of-fit (QFIT) value higher than the 85th percentile of 0.5 mag wide intervals (using m_{F625W}). Stars with a QFIT higher than 0.99 are always included, and stars with a QFIT lower than 0.9 are always excluded. The QFIT parameter describes how well the used point-spread-function model describes the flux distribution of each source. A value close to 1 indicates good agreement.
3. A ratio of flux from neighboring stars within the fit aperture over the flux of the star smaller than 0.5.

The combined cuts above already provide us with a reliable subsample. To ensure high and consistent quality throughout the whole magnitude range, we add one last, magnitude-dependent criterion: For both proper-motion components, we require the proper-motion error to be within the lower 95% of the error distribution in 0.5 mag wide intervals (see Figure 1, left). As can be seen in Figure 1, this selection tracks the magnitude dependence of the bulk of all well-measured stars, while excluding outliers with unusually high errors. One can also see that, at a magnitude of $m_{\mathrm{F625W}} = 24$, the upper limit on the errors reaches an order of magnitude of $0.3\,\mathrm{mas\,yr^{-1}}$ ($\sim 7.8\,\mathrm{km\,s^{-1}}$). As this is similar to half of the typical velocity dispersion in the outer regions of our studied field, we exclude stars fainter than this magnitude limit. Including stars with errors similar to the actual velocity dispersion would complicate the determination of the velocity dispersion and make it quite sensitive to the modeling of the proper-motion errors.

2.2. Spectroscopic Quality Selections

For the spectroscopic catalog, we defined the following criteria to create a well-measured subset of the data:

1. We require that each star matches the standard quality criterion defined in Paper I. This combined criterion contains cuts in the quality and reliability of the spectral fit, the accuracy of the recovered magnitude, the average signal-to-noise ratio, and the cluster membership. We further restrict the kinematic subsample to measurements with a relative mag accuracy `mag_rel`> 0.9 and a reliability parameter `rel`> 0.9. This helps to remove stars that are influenced by neighboring sources and may bias the kinematic measurements.
2. Similar to the HST-based proper motions, we rejected measurements whose line-of-sight velocity errors were larger than the 95th percentile in 0.5 mag wide bins (see Figure 1, right).
3. We set an overall magnitude cutoff at $m_{\mathrm{F625W}} > 18$. At this magnitude, our magnitude-dependent error cutoff reaches a level of $\sim 7.7\,\mathrm{km\,s^{-1}}$ (equivalent to the $0.3\,\mathrm{mas\,yr^{-1}}$ cutoff of $m_{\mathrm{F625W}} = 24$ for the proper-motion measurements).
4. We also require a successful crossmatch with the HST-based catalog (this was achieved for 307,030 of 342,797 stars from the MUSE catalog; see Paper II) and a high-quality HST-based measurement. This effectively makes the MUSE sample a subset of the HST sample and allows us to apply the same membership selections. In addition, it makes the MUSE subset a true 3D sample, allowing us to compare the results for both proper-motion-based and LOS-based measurements. The final MUSE sample contains 32,092 stars with a high-quality LOS measurement.

2.3. Cluster Membership Selection

To restrict our sample to likely cluster members and exclude fore- and background sources, we use both a photometric and a proper-motion-based criterion. First, we require that the stars lie on the red-giant branch or the main sequence in the F625W-F814W color–magnitude diagram using two manually defined fiducial lines (see Figure 2, left). This excludes cluster stars on the horizontal branch; however, their numbers are comparatively low and no MUSE line-of-sight velocities were measured for them. The other criterion is a global cutoff in total proper motion of $4.5\,\mathrm{mas\,yr^{-1}}$. This corresponds to around $115\,\mathrm{km\,s^{-1}}$, around 5.5 times higher than the typical velocity dispersion for main-sequence stars in the center of ω Cen. There is a small number of stars that pass this criterion but are likely nonmembers (see stars in upper right of the vector-point diagram in Figure 2). These sources are removed with an additional sigma-clipping step when determining the actual kinematic properties.

2.4. Summary of Selections

From an initial number of 1,395,781 stars with a proper-motion measurement, 669,975 pass our combined quality selection criteria, of which 610,846 then pass the subsequent membership cuts, constituting our proper-motion sample.

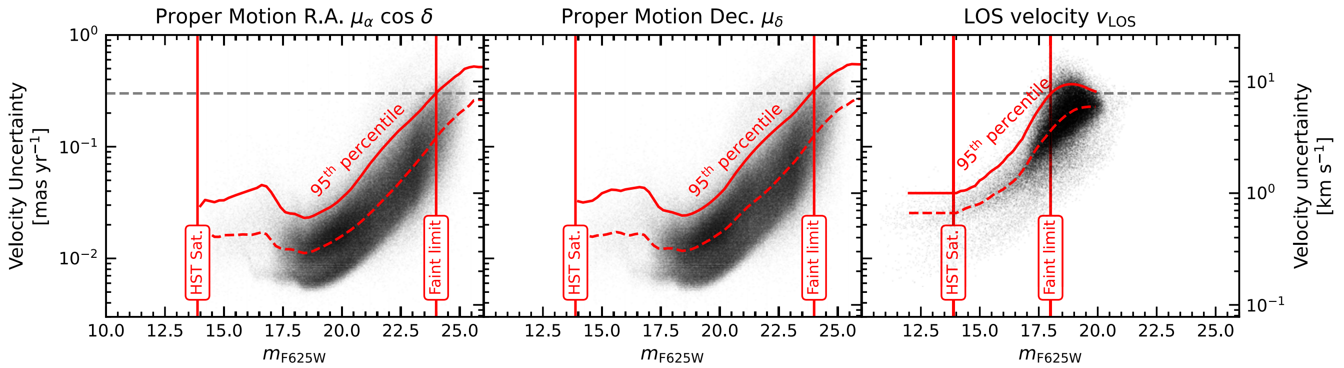

Figure 1. The three panels show the uncertainty of the individual velocity measurements for both the two proper-motion directions and the line-of-sight direction plotted against the magnitude in the $m_{\rm F625W}$. The red line marks the 95th percentile of the error distribution determined in 0.5 mag wide bins; it is used to reject stars with unusually large proper-motion errors. The dashed line marks the median of the error distribution. To facilitate comparisons between the proper motion and the line-of-sight uncertainties, all three panels have the same y-scale: the left axis shows astrometric units, and the right axis shows physical units at an assumed distance of 5494 pc (this leads to a conversion of 1 mas yr^{-1} = 26.06 km s^{-1}).

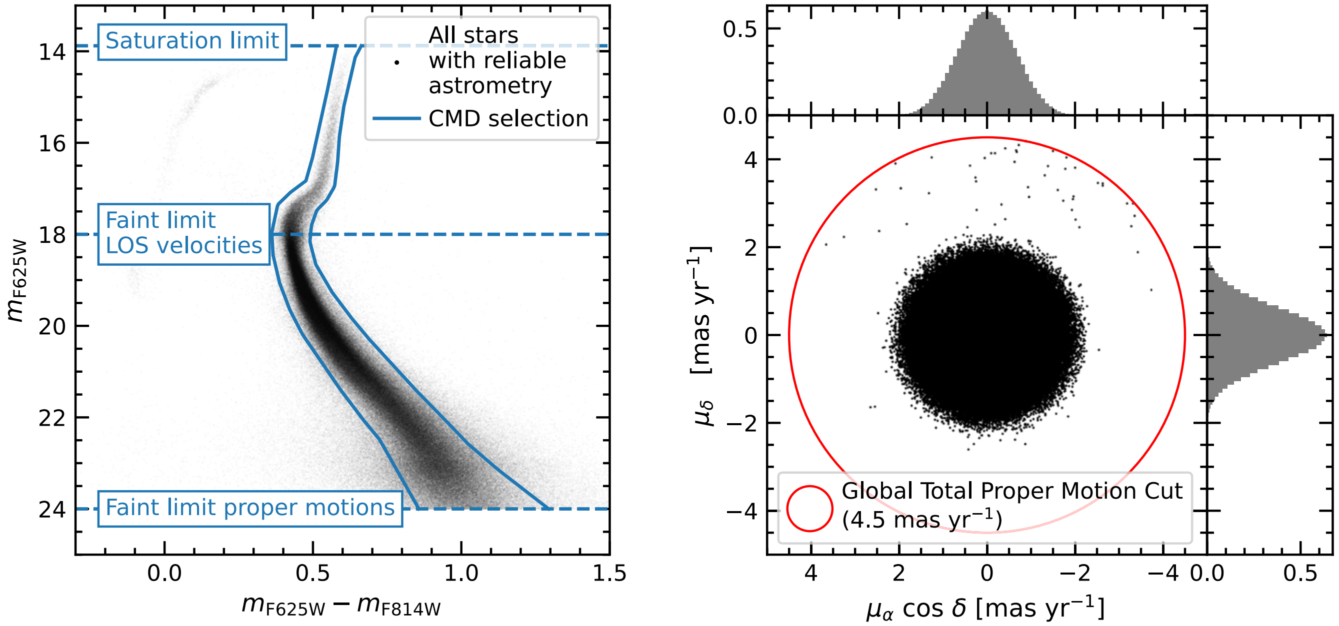

Figure 2. Left: A color–magnitude diagram based on photometry in the $m_{\rm F625W}$ and the $m_{\rm F814W}$ filter for all stars that pass the basic quality selections for the subsample used for the kinematic analysis. The blue solid lines mark our selection of main-sequence and red-giant-branch stars that are members of ω Cen. The dashed lines mark the bright and faint limits of the subsample used for the kinematic analysis. Right: A vector-point diagram of the stars in the high-quality subsample. The red circle marks the global proper-motion cutoff of 4.5 mas yr^{-1}. Stars with a total proper motion higher than this value are excluded from the kinematic analysis, as they are likely fore- or background stars. The histograms in the side panels show the marginalized distributions of the two proper-motion components.

From 342,797 stars with a line-of-sight velocity, 307,030 were successfully cross-matched with the HST catalog, of which 32,092 passed all spectroscopic quality criteria. Finally, 24,928 stars have both a high-quality astrometric and photometric measurement. The different selections are made available along with the data products (see also Table 1). The full 3D sample of velocities is shown in a three-dimensional version of a vector-point diagram in Figure 3. This Figure shows that all three velocity components show a similar distribution when assuming a distance of $d = 5494$ pc (our best-fit kinematic distance; see Section 3.5).

3. One-dimensional Profiles of the Kinematic Parameters

3.1. Determination of the Velocity Dispersion

The observed velocity distribution for both proper motions and LOS velocity is a superposition of the true velocity distribution and the measurement errors. To measure the underlying velocity dispersion we used the log-likelihood function for a Gaussian distribution with heterogeneous errors in the form presented by C. Pryor & G. Meylan (1993):

$$LL = -\frac{1}{2}\sum_i \left(\frac{(v_i - \bar{v})^2}{(\sigma^2 + \sigma_i^2)} + \log(2\pi(\sigma^2 + \sigma_i^2))\right), \qquad (1)$$

with $\bar{v}$ being the mean velocity in a certain subsample, σ being the true velocity dispersion, and v_i and σ_i being the individual stellar velocity measurements with their uncertainties. We sampled the likelihood function using the Markov Chain Monte Carlo code `emcee` (D. Foreman-Mackey et al. 2013b), using flat priors and 12 walkers with 500 steps each. We use the median of the posterior distribution as our best estimate for the velocity dispersion and use the 16th and 84th percentile as measures of the uncertainty.

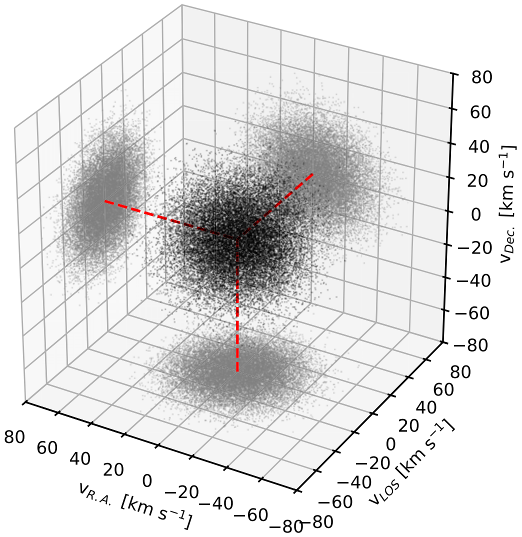

Figure 3. Three-dimensional vector-point diagram for the 24,928 stars that match both our proper motion and line-of-sight velocity quality criteria. Proper motions have been converted to physical velocities using our new kinematic distance of d = 5494 pc.

3.2. Proper-motion-based 1D Profiles of the Velocity Dispersion

To measure spatial variations of the velocity dispersion the data is typically split into radial bins. Several binning schemes are possible, and there is a tradeoff between spatial resolution, stochastic noise, and ease of presentation. We compare several binning schemes in Appendix D, but choose an adaptive logarithmic binning scheme as our standard. The radii of successive bins are increased by a factor of at least $10^{0.05} \approx 1.122$, while maintaining a minimum number of 100 stars per bin.

For all radial profiles and for the decomposition of the proper motions in radial and tangential components, we adopt the photometric center of the cluster as determined by J. Anderson & R. P. van der Marel (2010), with `R.A. = 13:26:47.24h` and `Dec. = -47:28:46.45°`. This center is independently confirmed by the presence of fast-moving stars (M. Häberle et al. 2024a) and by the kinematic center estimate performed in this work (see Section 4.2).

For the overall (combined) proper-motion dispersion $\sigma_{\mathrm{PM,c}}$, we treat the radial and tangential components of the proper motion as separate samples from the velocity distribution, which doubles the number of measurements. The resulting profile is shown in Figure 4, and the individual numerical values can be found in Table 2 (Appendix A). The velocity dispersion rises steadily from 0.52 mas yr^{-1} (13.6 km s^{-1}) at large radii to the central 10″, where it reaches a mean value of ∼0.81 mas yr^{-1} (21.1 km s^{-1}). The error bars at large radii are as small as 0.001 mas yr^{-1}, but they are higher near the center, due to the smaller number of stars per bin.

3.2.1. Comparison with Literature Profiles

The previous most widely used profile of the proper-motion dispersion in the inner region of ω Cen has been published in L. L. Watkins et al. (2015a) (hereafter Watkins15). In Figure 5, we compare the literature profile with our new profile. For the comparison, we have to take into account that the Watkins15 profile is based on a subset of bright stars. Due to the partial energy equipartition in the core of ω Cen, we expect a higher dispersion measured from our catalog, as we include lower-mass stars in the analysis. To allow for a consistent comparison, we also calculated a profile using only stars brighter than $m_{\mathrm{F625W}} = 19$, a threshold similar to the one used in Watkins15 and using a similar binning scheme.

The comparison of the profiles (Figure 5, middle panel) matches our expectations: Due to the significantly larger number of included measurements, both the spatial resolution and the individual errors in the new dispersion profile are improved when all well-measured stars from the new proper-motion catalog are used. Our profile shows less scatter and extends to larger radii. At larger radii, it shows slightly larger dispersion values, as expected from energy equipartition arguments: Using the same technique as in Section 6, we derive a mean stellar mass of 0.675 $M_\odot$ within the Watkins15 sample and of 0.515 $M_\odot$ within our full sample (that is spanning all magnitudes). Using the central energy equipartition value of $\eta = 0.08$ (Section 6) and Equation (3) predicts a 2% larger velocity dispersion when using the full sample.

When comparing a similar sample of bright stars (Figure 5, top panel) we see similar errors in the dispersion measurements (as these errors are dominated by the limited number of available stars in each bin and not on the individual proper-motion measurement errors) and overall agreement between the two profiles. However, we notice an overall smaller dispersion in all but the two innermost bins. One potential explanation could be a small underestimation of the proper-motion errors in the literature work, leading to an overestimation of the velocity dispersion.

3.3. Velocity Anisotropy Profiles

To study the velocity dispersion anisotropy, we decompose the proper-motion measurements into their radial and tangential components (with respect to the J. Anderson & R. P. van der Marel 2010 cluster center). As there are no strong correlations between the measurements in the R.A. and decl. components, we can treat them as independent measurements and calculate the errors on the projected components accordingly. We then calculate the dispersion profile for the two components separately (Figure 4, middle panel). While there are no apparent differences in the central regions, at larger radii, the radial velocity dispersion ($\sigma_{\mathrm{PM,rad}}$) is significantly higher than the tangential velocity dispersion ($\sigma_{\mathrm{PM,tan}}$). To quantify this, we also calculate the ratio between the two dispersion values $\sigma_{\mathrm{PM,tan}}/\sigma_{\mathrm{PM,rad}}$; see bottom panel in Figure 4. We find no significant anisotropy within $r < 30''$; after that, the velocity distributions become increasingly radially anisotropic, reaching $\sigma_{\mathrm{PM,tan}}/\sigma_{\mathrm{PM,rad}} = 0.0849 \pm 0.003$ at 281″ close to the half-light radius.

There is good agreement between our new measurements and the anisotropy profiles derived in Watkins15 (see bottom panel of Figure 5). However, the new measurements reach significantly larger radii.

3.3.1. Comparison with Other Clusters

M. Libralato et al. (2022) derived detailed kinematics for a large sample of Milky Way globular clusters and related the velocity dispersion anisotropy at the half-light radius with the half-light radius relaxation time (see their Figure 6). With an anisotropy value of $\sigma_{\mathrm{PM,tan}}/\sigma_{\mathrm{PM,rad}} = 0.0849 \pm 0.003$, the half-

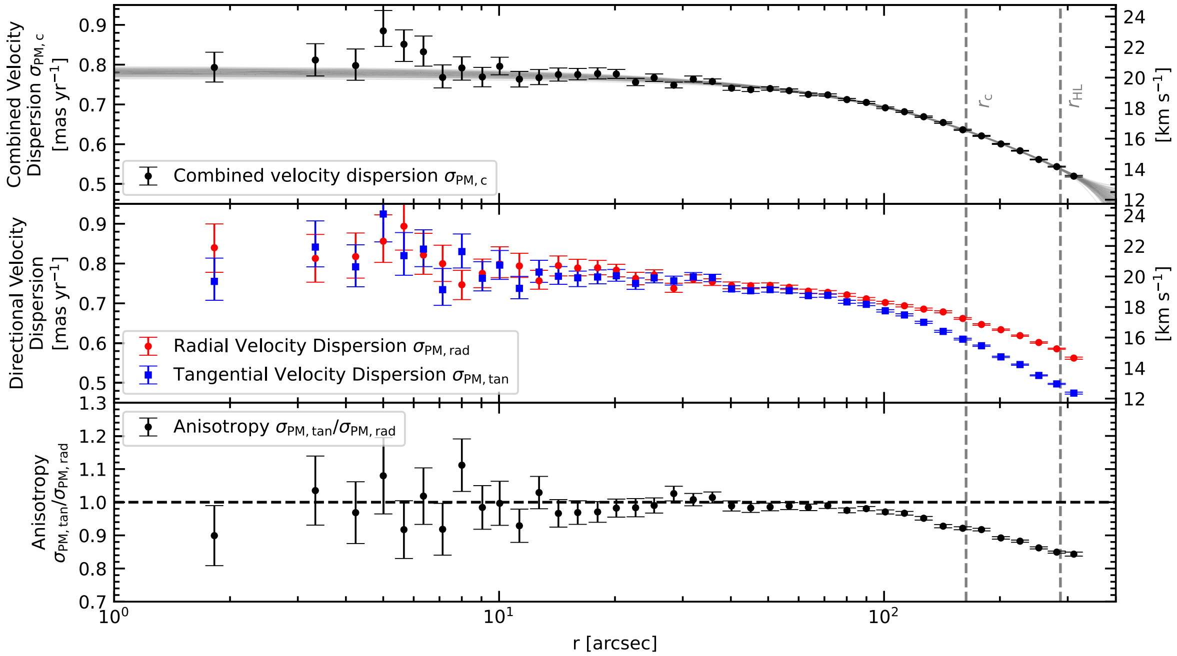

Figure 4. Proper-motion dispersion profiles determined using the new oMEGACat data using the full magnitude range. The profiles were determined using an adaptive logarithmic binning scheme with a step size of $\Delta \log r = 0.05$ and a minimum number of 100 stars per bin. The dashed vertical lines indicate the core and the half-light radii as reported in H. Baumgardt & M. Hilker (2018) Top: Overall dispersion, for which measurements of the tangential and the radial component of the proper motion were combined. The gray line shows the result of 100 fourth-order polynomial fits to the dispersion profile and is meant for visualization purposes only. Center: Individual components of the proper-motion dispersion in which the tangential and the radial components were treated separately. Bottom: Anisotropy profile calculated as the ratio between the tangential and the radial proper-motion dispersion component.

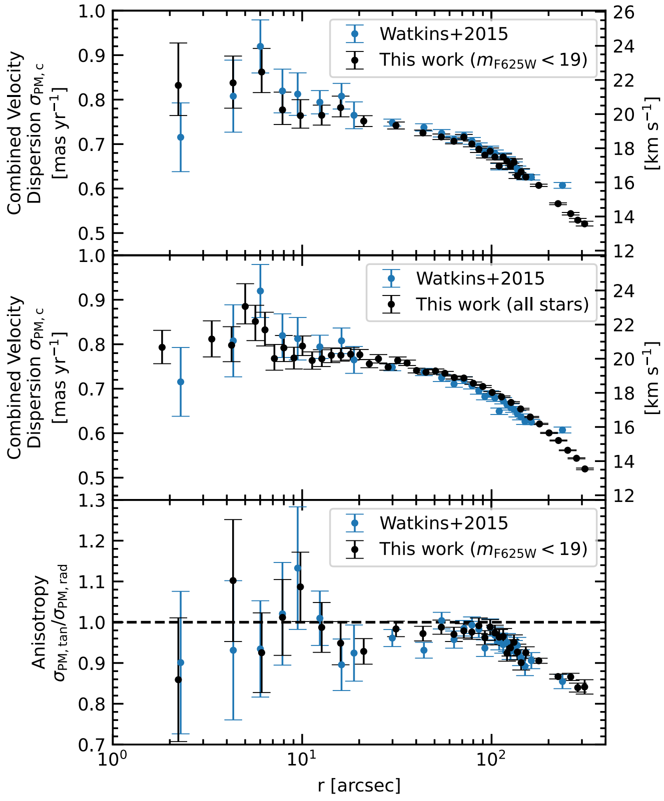

Figure 5. Proper-motion dispersion profiles determined using the new oMEGACat (black markers). We compare the new dispersion measurements with the literature profile by Watkins15 (blue markers). For better comparability, in the top panel, we restrict our data set to bright stars and use a binning scheme similar to the literature. In the center panel, we use logarithmic radial bins and the full high-quality subset. In the bottom panel, we compare the anisotropy, again using the bright sample only.

light anisotropy in ω Cen is significantly lower than for most other Milky Way globular clusters. Due to its young dynamical age (half-mass relaxation time ∼21 Gyr; H. Baumgardt & M. Hilker 2018), it still follows the trends presented in M. Libralato et al. (2022).

3.4. Dispersion and Rotation Profiles Based on the LOS Data

Unlike the proper motions, which have been measured relative to the bulk motion of the cluster and therefore do not contain any rotation signal, the line-of-sight velocity measurements are absolute and do show the rotation. Thus, the velocity dispersion and the rotation profile have to be determined simultaneously. We do this using the method developed in S. Kamann et al. (2018), which simultaneously fits for the velocity dispersion σ_{LOS}, the rotation v_{LOS}, and the position angle of the rotation axis θ_0 in each bin.

Again, we use an adaptive logarithmic binning scheme ($\Delta \log r = 0.05$, $N_{\min} = 50$) to split the data into circular bins. The resulting dispersion and rotation curves of the LOS velocities are shown in Figure 6 and in Table 3 (Appendix A).

The measured rotation curve starts with relatively high values in the innermost bins (although with uncertainties as large as $\sim 5\,\mathrm{km\,s^{-1}}$ due to the small number of measurements) before reaching a minimum at around $r = 30''$. Afterward, it increases monotonically until reaching a plateau with $v_{\mathrm{rot}} = 7\,\mathrm{km\,s^{-1}}$ at around $r = 150''$. The mean value of the position angle of the rotation axis for $r > 30''$ is $\theta_{\mathrm{LOS}} = (104.3 \pm 1.4)^\circ$.

The initial decrease of the rotational velocity is likely related to the counter-rotating structure discovered in R. Pechetti et al. (2024), as also indicated by the flip of the rotation angle (see Figure 6, right). The constant rotation velocity at radii larger than $r = 150''$ is also observed in the plane-of-sky rotation (see

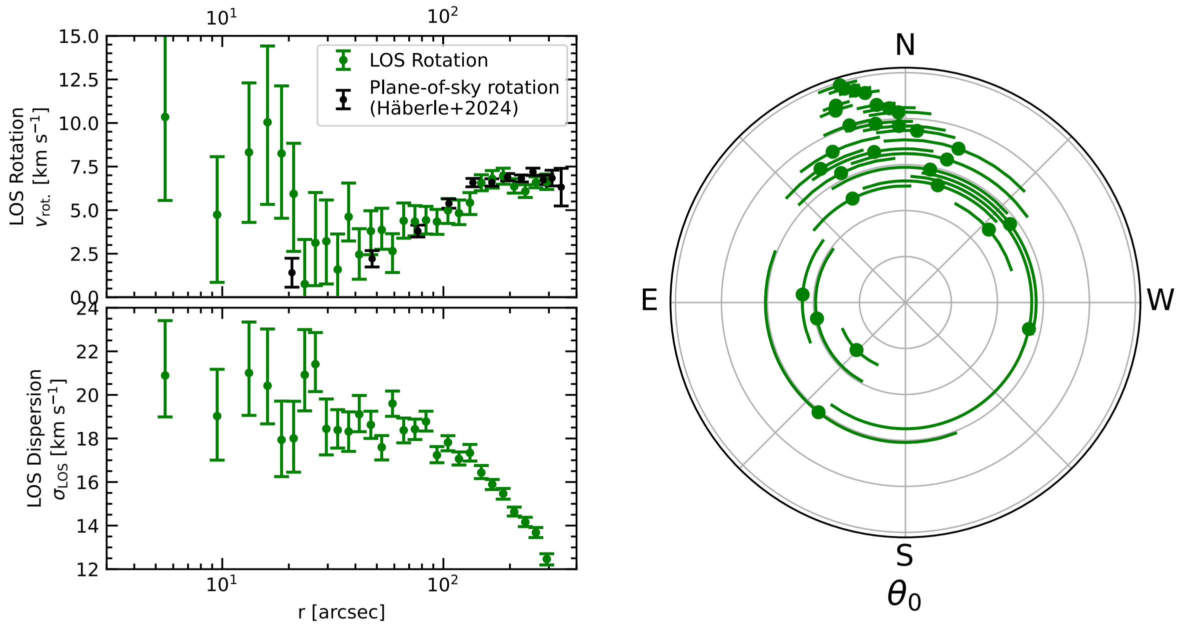

Figure 6. Top left: Rotation profile determined using the line-of-sight velocities. We compare our new LOS rotation profile with the plane-of-sky rotation curve presented in M. Häberle et al. (2024a) and find good agreement. Bottom left: Line-of-sight velocity dispersion profile. Right: Result for the position angle of the determined rotation axis.

M. Häberle et al. 2024a), as shown by the comparison in Figure 6. The similar rotation amplitudes of the different spatial components are expected due to the inclination of $i = 43.^\circ 9 \pm 1.^\circ 3$, as determined in M. Häberle et al. (2024a).

3.5. Comparison between Proper-motion and Line-of-sight Dispersion Profiles and Kinematic Distance

As the kinematic LOS sample is a subset of the proper-motion sample, we can also calculate the proper-motion profile using the same stars for all dimensions. This allows us to determine the kinematic distance of ω Cen, but also to capture potential systematic effects in either data set.

We use the following equation to obtain a kinematic distance estimate for each individual bin of the line-of-sight velocity dispersion profile, assuming that the proper-motion dispersion and the line-of-sight velocity dispersion are the same:

$$d\ [\mathrm{pc}] = (210.51\ [\mathrm{pc\ km^{-1}\ s\ yr^{-1}}]) \cdot \frac{\sigma_{\rm LOS}\ [\mathrm{km\ s^{-1}}]}{\sigma_{\rm PM,c}\ [\mathrm{mas\ yr^{-1}}]}. \quad (2)$$

The upper panel of Figure 7 shows a comparison between the proper-motion dispersion ($\sigma_{\rm PM,c}$) and the line-of-sight velocity dispersion ($\sigma_{\rm LOS}$) using a distance of 5494 pc, the best-fit distance described below. The two profiles show good agreement within their error bars for most of the bins. In the lower panel of Figure 7, we compare the line-of-sight profile with the radial and tangential components of the proper-motion dispersion. At larger radii, where the velocity anisotropy is more pronounced, one can see that the line-of-sight dispersion falls in between the radial and tangential proper-motion dispersion profile. This can be explained geometrically: the LOS velocities contain both a radial and a tangential component, depending on the (unknown) LOS position of the star.

The results for the kinematic distance are shown in Figure 8. To limit the influence of the anisotropy on the kinematic distance estimate, we restrict our analysis to the inner region of ω Cen ($r < 100''$), for which the velocity dispersion is approximately isotropic (see Figure 4). The variance weighted mean of all individual kinematic distance estimates within our cutoff radius is (5494 ± 61) pc. This value is in 1σ agreement with the value of (5430 ± 50) pc determined in H. Baumgardt & E. Vasiliev (2021) by averaging several different distance estimation methods (see their paper for a detailed comparison of various other literature distance estimates). As our estimate is based on a consistent data set (with the same large sample of stars with both well-measured proper motions and LOS velocities), we consider it the most reliable available kinematic distance value, in addition to being one of the most precise distance measurement of any kind available for ω Cen. An overview of various other distance estimates, including Gaia parallaxes, is given in Table 4 in the Appendix A.

We note that our simple method of estimating the kinematic distance requires the assumption of isotropy between the proper motion and the line-of-sight velocity components, which is why we restrict ourselves to radii $r < 100''$. In this inner region, the anisotropy is close to one ($\sigma_{\rm PM,tan}/\sigma_{\rm PM,rad} \geqslant 0.97$). At larger radii, we expect some bias due to anisotropy and flattening of the velocity field (see also G. van de Ven et al. 2006). The lower kinematic distance values for the bins at larger radii (see Figure 8) might be caused by this effect; the weighted mean for the kinematic distance using all available bins is (5445 ± 41) pc. The Gaia kinematic distance estimate from H. Baumgardt & E. Vasiliev (2021) of (5359 ± 141) pc is derived from data at predominantly larger radii than our estimate, and is therefore independent of our value. The consistency in the derived distance therefore adds further credibility to our estimate and suggests our kinematic distance is reliable. However, modeling of the oMEGACat data based on an accurate anisotropic, rotating, and flattened model fit to the data could result in an improved estimate and will be subject of a future paper.

4. Kinematic Maps

The large number of stellar measurements in the new oMEGACat catalogs allows us to derive kinematic maps with fine spatial resolution and large spatial coverage.

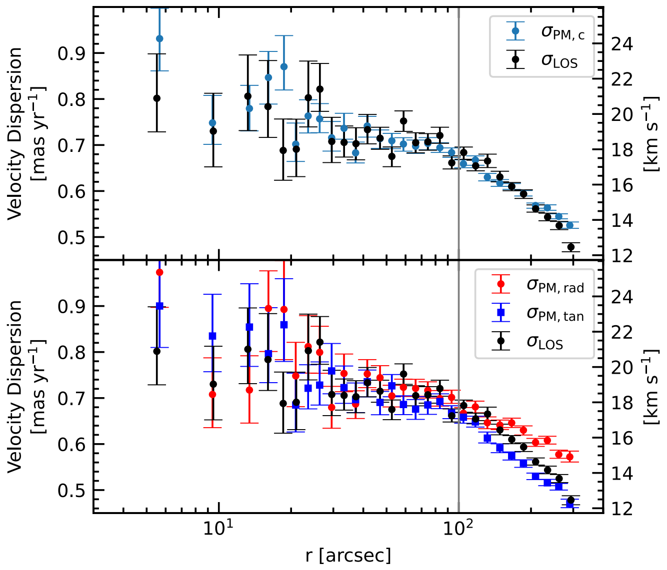

Figure 7. Top: A comparison between the line-of-sight velocity dispersion profile and the overall proper-motion dispersion. A distance of 5494 pc was assumed to convert between proper motions and physical velocities. The two profiles show good agreement. Bottom: A comparison between the line-of-sight velocity dispersion and the individual (radial and tangential) components of the proper-motion dispersion. At larger radii ($r > 100''$; gray vertical line), where the proper-motion field turns increasingly radially anisotropic, the line-of-sight velocity dispersion lies in between the two different proper-motion profiles.

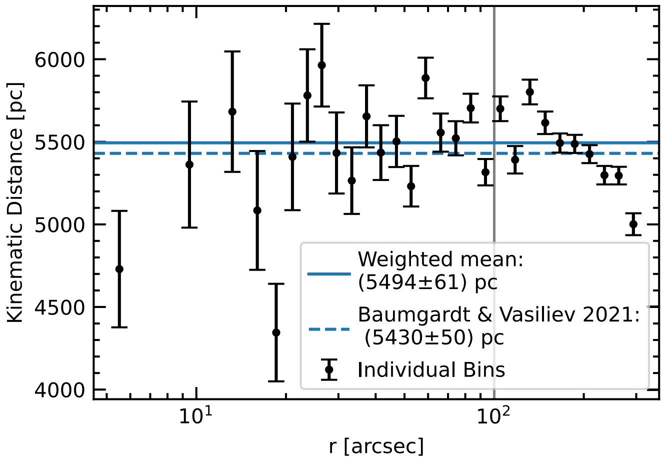

Figure 8. Kinematic distance of ω Cen derived by calculating the ratio between line-of-sight and proper-motion dispersion in different circular bins (see also Figure 7, top). We restrict the calculation of a weighted mean velocity to the region $r < 100''$ (gray vertical line), to limit the influence of anisotropy. The weighted mean value is in good agreement with the literature distance value derived in H. Baumgardt & E. Vasiliev (2021).

4.1. Maps of the Total Proper-motion Dispersion

To create velocity dispersion maps of the proper motion, we use the Python Voronoi binning package `vorbin` (M. Cappellari & Y. Copin 2003) to separate the field into approximately equally populated two-dimensional bins. We set a target number of 250 stars per bin, which yields a median uncertainty of approximately 0.02 mas yr^{-1} (≈ 0.5 km s^{-1}) per bin and a total number of 2434 bins. Figure 9 shows the resulting map of the combined velocity dispersion $\sigma_{\rm PM,c}$ with a zoom into the innermost arcminute. The map shows the overall decrease of the velocity dispersion toward larger radii and has an overall symmetric and smooth appearance, indicative of the large number and high quality of the underlying velocity measurements.

4.2. Empirical Fits of a Smooth Model

To determine the general geometric properties of the velocity dispersion map and a kinematic estimate for the cluster center, we fit a 2D Gaussian function to velocity dispersion values determined in the Voronoi bins. A single 2D Gaussian provides a decent fit (see Figure 10) with a reduced $\chi^2 = 0.99$ and independently recovers the cluster center (ΔR.A. $= -1\farcs31 \pm 0\farcs72$, Δdecl.$=1\farcs44 \pm 0\farcs66$) with respect to the photometric center determined in J. Anderson & R. P. van der Marel 2010). The best-fit position angle is $\Theta = 101\fdg4 \pm 2\fdg4$ (counterclockwise offset of the major axis with respect to north), and the dispersion distribution is flattened along the minor axis of the cluster with $1 - \sigma_y/\sigma_x = 0.09$. The flattening of the velocity field is similar to the photometric flattening, where the mean ellipticity $\epsilon = 1 - \frac{b}{a} = 0.010$ (E. H. Geyer et al. 1983; E. Pancino et al. 2003; A. Calamida et al. 2020; see also Appendix D). The position angle also is in agreement with the photometric value (e.g., 100°; G. van de Ven et al. 2006) and with the rotation axis value found using LOS velocities ($\Theta_{0,\rm LOS} = 104\fdg3 \pm 1\fdg4$; see above).

Even though the global properties are well described by a single Gaussian, the residuals show that there is a significant rise of the velocity dispersion within $r < 10''$. Future dynamical models are necessary to interpret this further, but the size of this feature is comparable to the radius of influence of a $\sim$20,000 $M_\odot$ intermediate-mass black hole using the equation of P. J. E. Peebles (1972). Allowing a second Gaussian component (with the same center as the first component) in the fit model (see Figure 10, lower row) allows the model to describe this central rise in velocity dispersion and to further reduce the reduced χ^2 to 0.91. The kinematic center, the position angle, and the flattening of the outer component are still successfully recovered.

4.3. Maps of the Proper-motion Anisotropy

To study the two-dimensional variation of the velocity anisotropy, we use the same binning scheme as in the previous section but now calculate the two dispersion components ($\sigma_{\rm PM,rad}$ and $\sigma_{\rm PM,tan}$) separately; see Figure 11. While the overall velocity dispersion distribution shows only mild ellipticity, the radial velocity dispersion appears highly flattened with respect to the rotation axis of the cluster, and the tangential velocity dispersion appears to be elongated along the rotation axis. The 2D map of the anisotropy ($\sigma_{\rm tan}/\sigma_{\rm rad}$) shows the overall trend to radial anisotropy at larger radii, but also two "tangentially anisotropic" plumes along the rotation axis. This 2D structure can be naturally explained as a superposition of the actual physical anisotropy in the velocity dispersion and a geometric projection effect of the rotation of the cluster: In a 2D projection, stars that are close to the rotation axis preferentially move orthogonally to the axis, resulting in an apparent increase in the observed tangential velocity dispersion.

4.4. Maps of the Line-of-sight Mean Velocity and Dispersion

In Figure 12, we derive Voronoi-binned kinematic maps based on the line-of-sight velocity measurements. Due to the

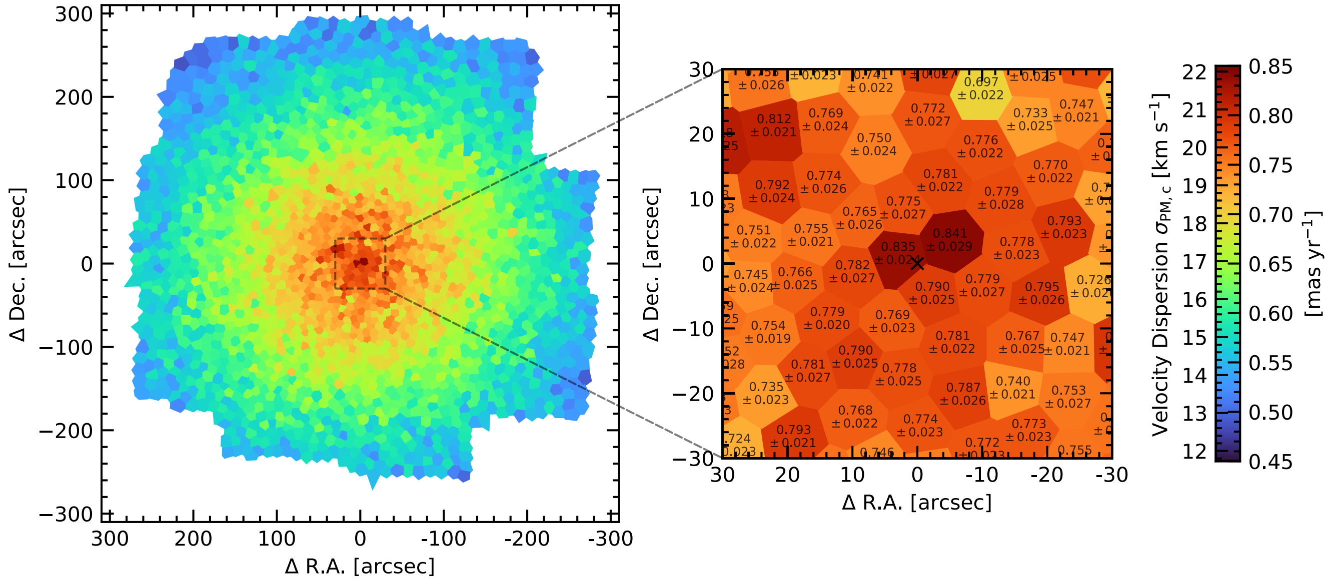

Figure 9. Dispersion map combining both proper-motion components and determined using $N = 250$ Voronoi bins. The right panel shows a zoom into the centermost arcminute with the numerical values (in mas yr^{-1}) for the individual bins shown in black letters.

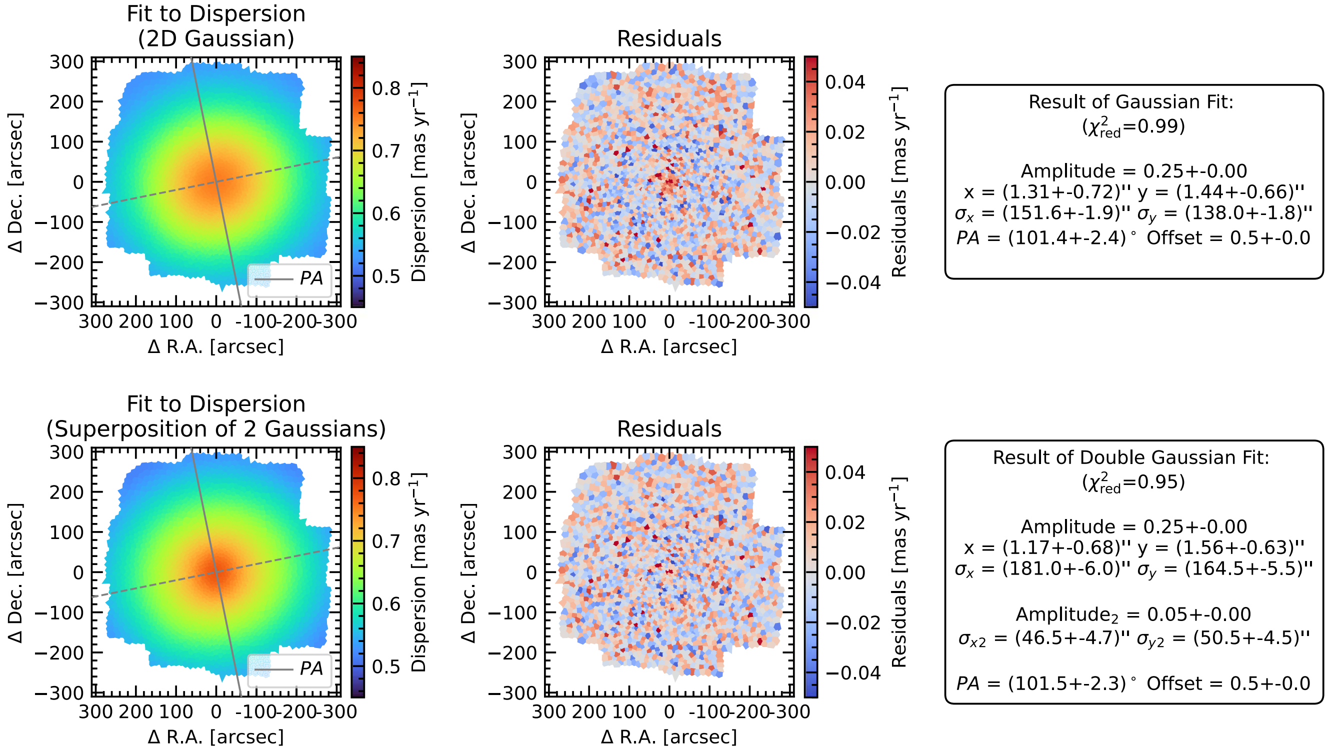

Figure 10. Top: Result of a single-component 2D Gaussian fit to the 2D proper-motion dispersion field shown from Figure 9. The left shows the result, the center shows the residuals, which are in good agreement besides an underestimation of the cusp of the velocity dispersion in the centermost region, and the right shows the parameters of the Gaussian fit. Bottom: Results for a two-component 2D Gaussian fit. This two-component model is better able to describe the velocity dispersion in the innermost region, as can be seen from the residuals. Both models successfully recover the ellipticity and the position angle of the dispersion field.

significantly smaller size of the LOS sample (24,928 sources compared to 610,846 sources in the proper-motion sample), we have resorted to a smaller target bin size of $N = 100$ stars per bin. This still leads to larger bins compared to Figure 9.

6Opposite to the proper-motion measurements (which by construction have a zero mean motion), the line-of-sight velocities contain the rotation signal of the cluster. Therefore, we show both the mean line-of-sight velocity per bin (Figure 12, left) and the derived velocity dispersion σ_{LOS} (Figure 12, right). The mean velocity map nicely shows the line-of-sight rotation pattern. The dispersion map looks similar to the maps derived with the proper motions, but it shows larger scatter (as expected due to the smaller sample size). We performed a 2D Gaussian fit to the dispersion field (Figure 13), which showed a reduced χ^2 value similar to those of the proper-motion maps. This fit again recovered the cluster center and the position angle (compare with Figure 10), albeit with larger statistical errors. Contrary to the case of the velocity

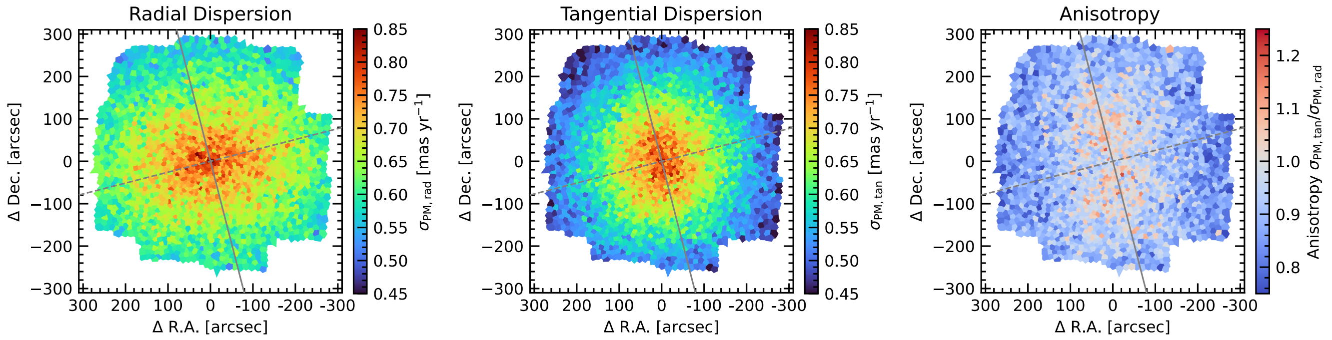

Figure 11. Proper-motion dispersion maps determined separately for the radial (left) and the tangential (center) proper-motion component. These individual-component velocity fields show strong flattening/elongation along the rotation axis (solid gray line) of the cluster, which is likely a geometric effect. The ratio of the two components (right) gives a measure of the anisotropy of the velocity fields. At larger radii, the field becomes increasingly radially anisotropic. In addition, there are two tangentially anisotropic plumes along the rotation axis.

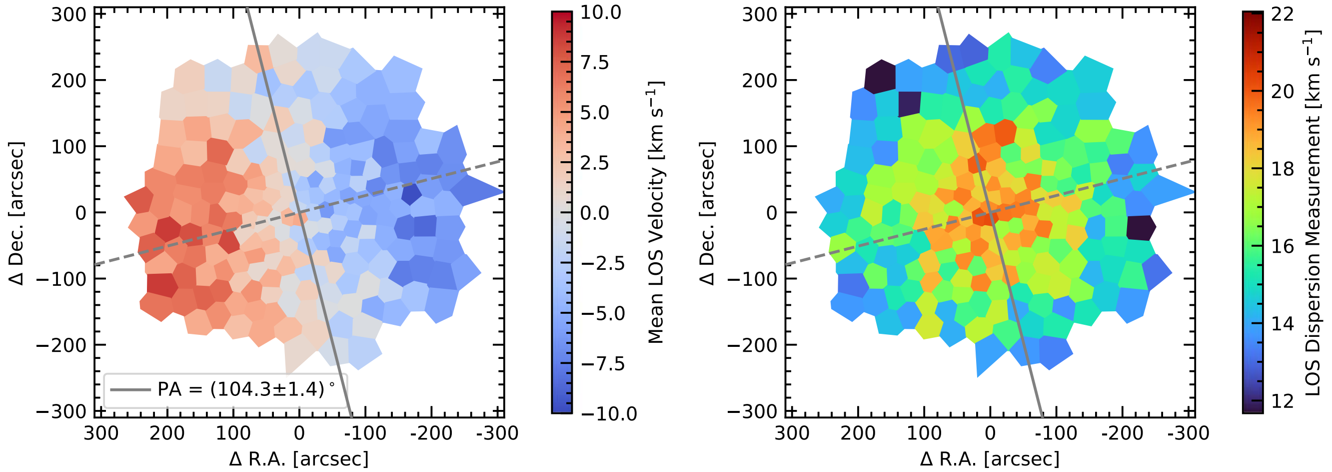

Figure 12. Left: Mean line-of-sight velocity determined in $N = 100$ Voronoi bins. The global rotation of ω Cen is clearly visible. Right: Line-of-sight velocity dispersion determined in Voronoi bins.

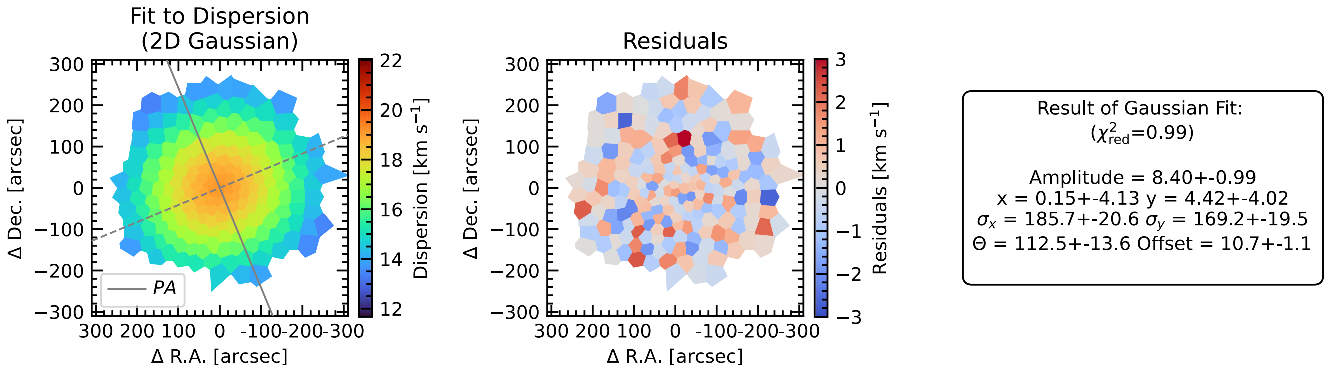

Figure 13. Result of a 2D Gaussian model fit to the line-of-sight velocity dispersion map (compare with Figure 10). Left: Best-fit Gaussian model Center: Residuals Right: Parameters of the fit.

dispersion map, a second Gaussian component did not improve the fit (likely due to the larger bin sizes and statistical uncertainties).

5. Search for Metallicity-dependent Kinematics

It is well known that ω Cen hosts multiple stellar populations with a wide spread in metallicity (see introduction). Differences in the spatial distribution and the kinematics of the different subpopulations can help to constrain their origin (see M. Alfaro-Cuello et al. 2019, 2020; N. Kacharov et al. 2022, for the case of M54). Various papers have studied the spatial distribution of the different subpopulations in ω Cen. Early works using ground-based data (A. Sollima et al. 2007; A. Bellini et al. 2009) found an increase in the concentration of the helium-enhanced blue main sequence within the inner region of the cluster, while at larger radii ($r > 10'$) the ratio of the different helium abundance subpopulations remains approximately constant (however, A. Calamida et al. 2017 and A. Calamida et al. 2020 found evidence for a more extended distribution of the blue main-sequence stars). Most recently, M. S. Nitschai et al. (2024) found no radial variation of the stellar distribution with MUSE-based metallicity measurements

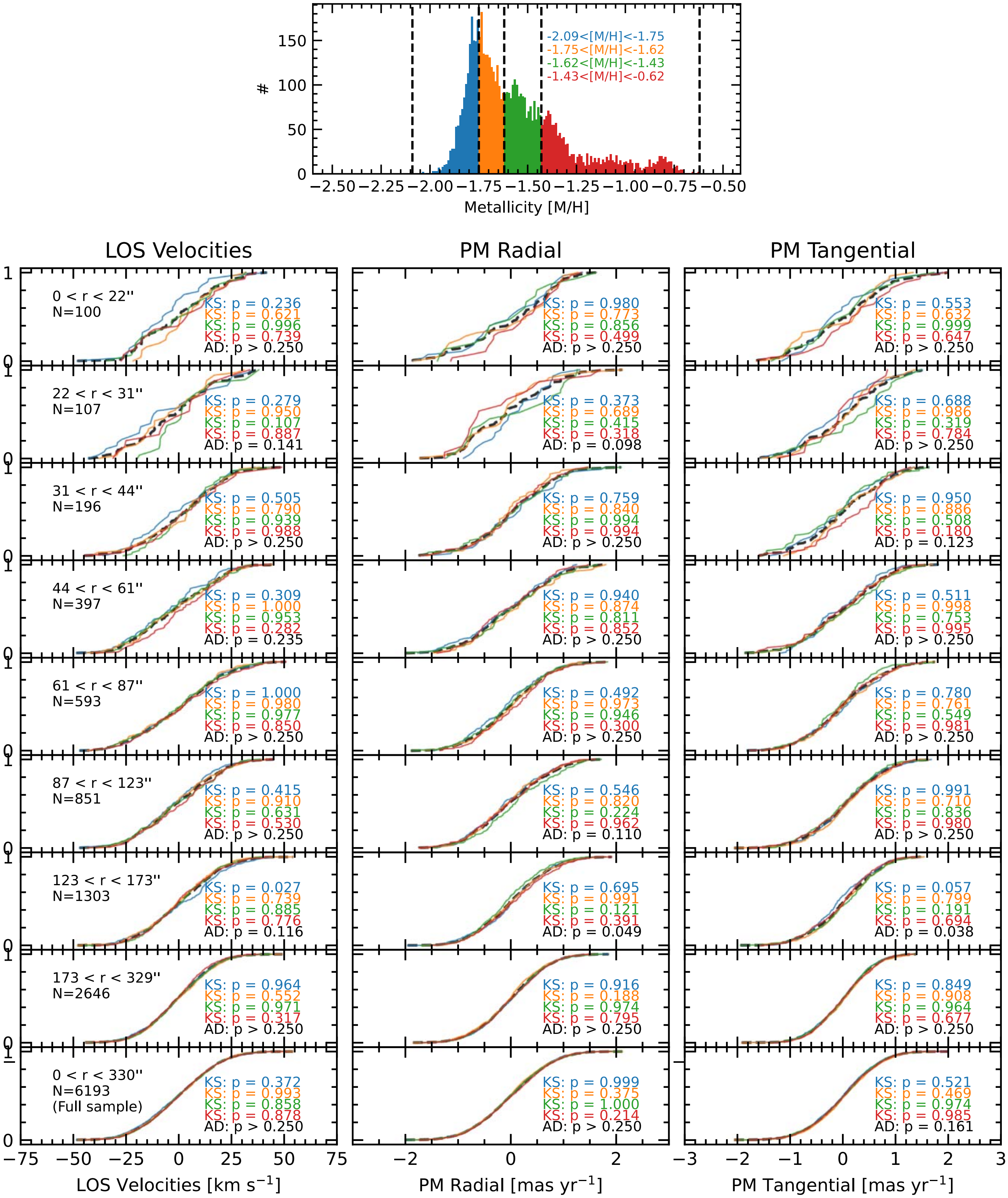

Figure 14. Top: Metallicity distribution for bright ($m_{\mathrm{F625W}} < 17$), well-measured stars in the catalog. We split the sample into metallicity quartiles indicated with different colors. Bottom: Normalized cumulative distribution functions for the three velocity components and for eight different radial bins. We compared the velocity distribution for each metallicity quartile with the overall velocity distribution (black dashed line) using a Kolmogorov–Smirnov (KS) and a k-sample Anderson–Darling (AD) test, but found no significant differences. The p-values for the null hypothesis are shown in each panel.

within the half-light radius, while M. Scalco et al. (2024) confirmed the trend of a more centrally concentrated blue main sequence from A. Bellini et al. (2009) with precise space-based photometry at larger radii ($\sim 1 - 3 r_{\mathrm{HL}}$).

The kinematics of the different subpopulations have been subject to several investigations: Exempli gratia, J. Anderson & R. P. van der Marel (2010) found no kinematic differences between the blue- and red-main-sequence populations in the

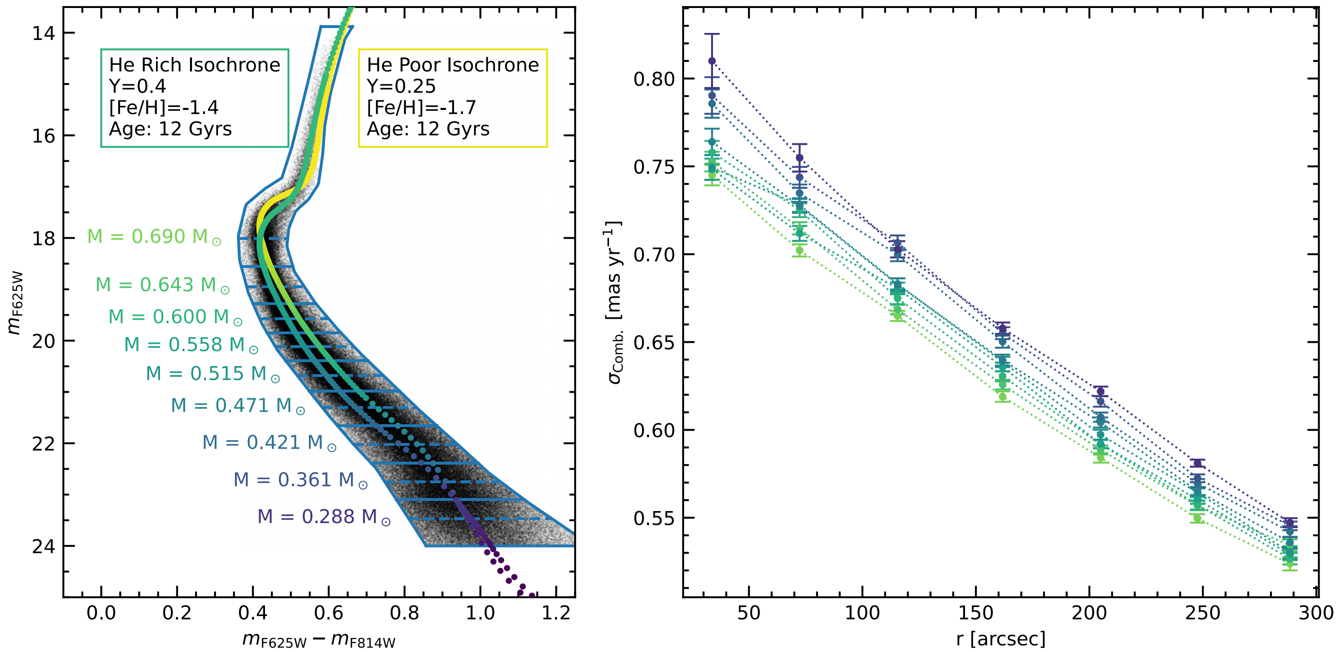

Figure 15. Left: m_{F625W}, m_{F814W} color–magnitude diagram used to split the data set in 10 equally populated $m_{\rm F625W}$ bins. For each bin, a weighted mean mass is estimated using two isochrones to account for both the helium-rich and helium-poor populations in ω Cen. Right: Combined velocity dispersion profile determined for the different mass bins and for seven different radial bins.

inner region of ω Cen. At larger radii ($\sim 3.5\, r_{\rm HL}$), A. Bellini et al. (2018) found significant differences between the anisotropy, the systemic rotation, and the state of energy equipartition for the different populations.

In this work, we focus on the bright end of the sample, where precise line-of-sight velocities and metallicity measurements are available. To do so, we further restrict the sample of 24,928 stars with a full 3D velocity measurement to $m_{\rm F625W} < 17$ (this limit is necessary to obtain reliable and bias-free metallicity; see M. S. Nitschai et al. 2024), which leaves us with a subset of 6193 stars. The metallicity distribution for this sample is shown in Figure 14 (upper panel). We then further split the data set into four quartiles in metallicity and search for differences in the velocity dispersion in different radial bins (again, we used an adaptive logarithmic binning scheme with $N_{\rm min} = 100$ and $\Delta {\rm Log}r = 0.15$) and for all three velocity components (LOS velocity, radial proper motion, and tangential proper motion); see Figure 14 (lower grid of plots). In each radial bin and for each velocity component, we run a Kolmogorov–Smirnov (KS) and a k-sample Anderson–Darling test to see whether the distribution of an individual metallicity quartile differed significantly from the total distribution. The p-values for the null hypothesis (i.e., that the samples are drawn from the same distribution) for both tests are shown in Figure 14. We do not find significant ($p < 0.05$) deviations between the distributions in any of the velocity components (radial and tangential proper motion, and LOS velocity) nor in any of our radial bins.

This is consistent with the picture of well-mixed populations within the half-light radius of ω Cen; see also M. S. Nitschai et al. (2024). It is also consistent with the recent results of N. Vernekar et al. (2025), who found no metallicity-dependent kinematics using both Gaia and the oMEGACat II HST data. More subtle kinematic differences between the subpopulations may still be discovered when using the full proper-motion sample instead of the sample limited to bright stars with a reliable spectroscopic metallicity measurement. This is the subject of a planned future project.

6. Energy Equipartition

Due to two-body relaxation processes, globular clusters evolve toward a state of energy equipartition, in which lower-mass stars show higher velocity dispersion than stars with higher masses (L. Spitzer 1969). Traditionally, the state of energy equipartition has been parameterized by fitting the parameter η, where the velocity dispersion σ shows the following dependence on the mass m:

$$\sigma \propto m^{-\eta}. \tag{3}$$

A value of $\eta = 0.5$ would mean full energy equipartition; however, N-body simulations show that globular clusters only reach partial energy equipartition (H. Baumgardt & J. Makino 2003; M. Trenti & R. van der Marel 2013).

A different parameterization of the state of energy equipartition using the so-called equipartition mass ($m_{\rm eq}$) was introduced in P. Bianchini et al. (2016) with the equation:

$$\sigma(m) = \begin{cases} \sigma_0 \exp\left(-\frac{1}{2}\frac{m}{m_{\rm eq}}\right) & \text{if } m \leqslant m_{\rm eq} \\ \sigma_{\rm eq}\left(\frac{m}{m_{\rm eq}}\right)^{-1/2} & \text{if } m > m_{\rm eq} \end{cases}, \tag{4}$$

where σ_0 indicates the velocity dispersion for massless particles and $\sigma_{\rm eq}$ corresponds to the value of velocity dispersion for $m = m_{\rm eq}$. The $m_{\rm eq}$ mass is a proxy for the level of partial energy equipartition reached by the system, such that, for $m > m_{\rm eq}$, the system is in full energy equipartition.

The state of energy equipartition is a measure for the overall evolutionary state of the cluster (A. T. Baldwin et al. 2016) and other underlying properties such as the presence of black holes, which can reduce the level of energy equipartition in the

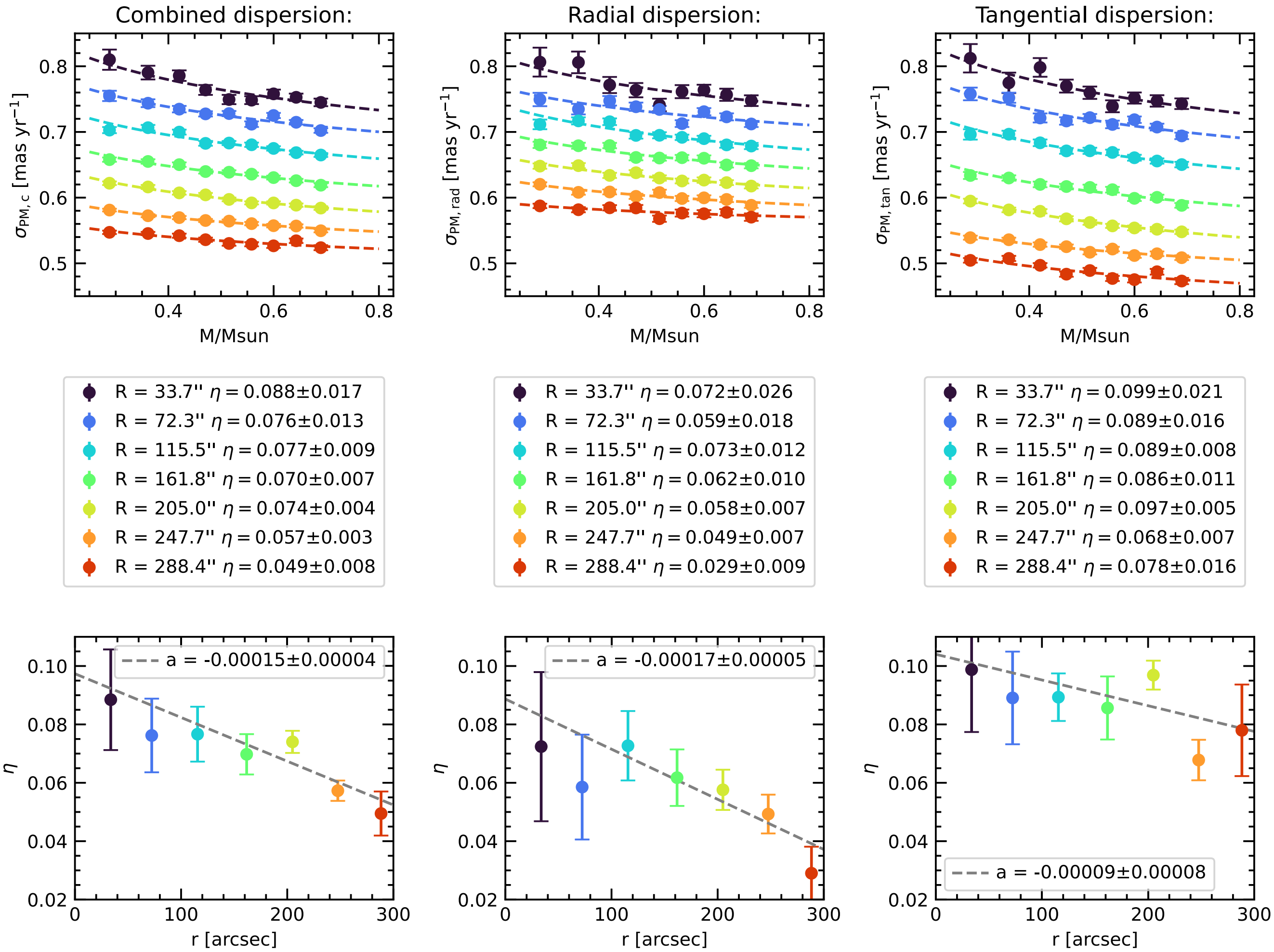

Figure 16. Top: Variation of the velocity dispersion with stellar mass. We compare the behavior of the combined velocity dispersion with the individual spatial components (left: combined velocity dispersion, middle: radial velocity dispersion, right: tangential velocity dispersion). The different colors show the measurements in seven different radial bins. The dashed line shows the best fit of the mass dependence using the classical η parameterization. In the middle row, we show the numerical values of the fit results, and in the bottom row, we show the radial behavior of the energy equipartition parameter. For both spatial directions, we can observe a decrease in the degree of energy equipartition with radius, indicated by a lower value of the parameter η. This trend is stronger for the radial component than for the tangential component.

luminous stars in the cluster (N. C. Weatherford et al. 2018; F. I. Aros & E. Vesperini 2023; N. Dickson et al. 2024). Initial anisotropy in the velocity distribution of a stellar cluster has been shown to influence how fast the system evolved toward energy equipartition (V. Pavlík & E. Vesperini 2021; V. Pavlík et al. 2024), with tangentially anisotropic systems showing a more rapid evolution. V. Pavlík & E. Vesperini (2022) further predict differences in the evolution toward energy equipartition for the projected radial and the tangential components of the velocity that can be measured via proper motions.

Observationally, the energy equipartition can be studied by comparing the velocity dispersion measured for stars in different mass bins. However, this is challenging due to the need for velocity measurements with reliable uncertainties over a wide range of stellar masses and magnitudes. While spectroscopic LOS velocity measurements are typically limited to bright evolved stars that have similar masses, HST-based proper-motion catalogs have recently enabled the study of energy equipartition in a variety of globular clusters (e.g., M. Libralato et al. 2018, 2022), including ω Cen (J. Anderson & R. P. van der Marel 2010; A. Bellini et al. 2018; L. L. Watkins et al. 2022). Due to its high precision and depth, the oMEGACat proper-motion catalog is perfectly suited to extend these existing studies to lower masses and wider radial coverage.

6.1. Estimation of Stellar Masses

As a first step for our energy equipartition studies, we split our high-quality proper-motion subset into nine equally populated magnitude bins (see Figure 15). Due to the complex stellar populations in ω Cen, it is not straightforward to directly infer stellar masses from their color–magnitude-diagram position. As we focus on the overall kinematics (and do not yet aim to study each subpopulation separately), we use the following approximation (adapted from A. Bellini et al. 2018, but with different weights for the different stellar populations) to determine the mean stellar mass in each magnitude bin: We use two different 12 Gyr isochrones representing the helium-rich and the helium-poor population of the main sequence to infer the mean mass for the different magnitude bins (see Figure 15, left). For each magnitude bin, we calculated the mean magnitude and interpolated the two isochrones to infer the corresponding stellar mass. We then combined the two different mass estimates, giving them an equal weight (due to their similar

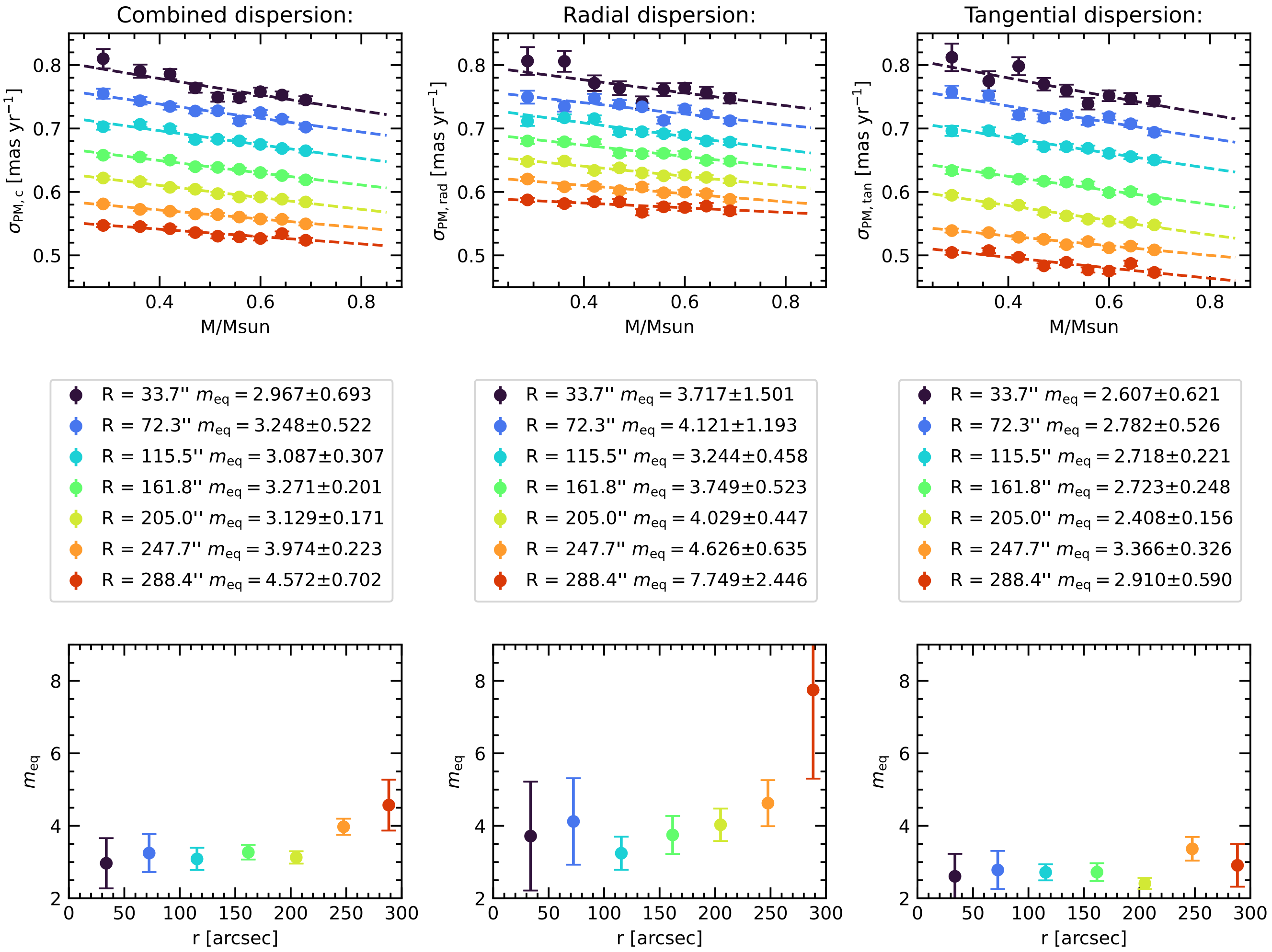

Figure 17. This figure is equivalent to Figure 16 and compares the spatial variability of the degree of energy equipartition for the different components of the proper motion. Instead of the η parameter, we use the energy equipartition mass (m_{eq}) parameterization (P. Bianchini et al. 2016) to quantify the degree of energy equipartition. A lower value of m_{eq} indicates a higher degree of energy equipartition.

fraction within the half-light radius; see A. Bellini et al. 2009). The isochrones were obtained using the Dartmouth Stellar Evolution Database (A. Dotter et al. 2007, 2008). We used the following parameters:

1. Helium-rich isochrone: $Y = 0.4$, [Fe/H] $= -1.4$ weight: 50%;
2. Helium-poor isochrone: $Y = 0.25$, [Fe/H] $= -1.7$ weight: 50%; and
3. Reddening: $E(B - V) = 0.16$.

The mean masses per bin in our sample extend from 0.288 $M_\odot$ to 0.690 $M_\odot$, a large range that was previously not accessible in the inner regions of ω Cen.

6.2. Variation of the Energy Equipartition with Radius

In addition to splitting our data set into different mass bins, we also split it into seven different annular radial bins (each with a width of 45″). This allows us to probe the state of energy equipartition at different radii of the cluster. For each magnitude and radial bin, we determine the proper-motion dispersion both for the combined proper motion but also the radial and tangential components individually. A plot showing the different dispersion profiles is shown in Figure 15 (right). In this plot, it can already be seen that the high-mass stars show lower velocity dispersion than stars with lower masses, indicative of at least some level of energy equipartition. In the next step, we fit the mass dependency of the velocity dispersion in each radial bin using either the classical η or the Bianchini m_{eq} parameterization. The results are shown in Figures 16 and 17.

We can make the following general observations: At all radii and for both proper-motion directions, we can observe at least some degree of energy equipartition. The energy equipartition is highest in the innermost bin ($\eta = 0.088 \pm 0.017$; $m_{\mathrm{eq}} = (2.97 \pm 0.69)\,M_\odot$) and decreases toward larger radii (at the half-light radius: $\eta = 0.049 \pm 0.009$; $m_{\mathrm{eq}} = (4.51 \pm 0.70)\,M_\odot$). This trend is consistent with measurements at significantly larger radii ($\eta = 0.030 \pm 0.019$; $r \sim 3.5\,r_{\mathrm{HL}} \sim 975''$); see A. Bellini et al. (2018).

6.3. Anisotropy in the Energy Equipartition

The overall trends measured for the combined velocity dispersion also hold for the individual radial and tangential directions. However, we can find the following differences between the two directions: While the degree of energy equipartition of the radial component quickly decreases with radius (and the radial velocity dispersion almost does not vary with mass at $r \approx r_{\mathrm{HL}}$; see Figure 16), the tangential component shows an overall higher degree of energy equipartition and a weaker dependence with radius. This is tentatively in line with recent simulation results (J. Pfeffer et al. 2021; V. Pavlík & E. Vesperini 2022; V. Pavlík et al. 2024) that find a faster evolution toward energy equipartition for the tangential component of the velocity.

7. Summary and Conclusions

We present a study of several basic kinematic properties of the massive globular cluster ω Cen based on the new spectroscopic and astro-photometric oMEGACat catalogs (PaperI; Paper II). Due to the enhanced radial coverage and precision of these catalogs and the unique three-dimensional combination of plane-of-sky proper motions and spectroscopically measured line-of-sight velocities, our analysis significantly improves the kinematic picture of ω Cen and can serve as input for future modeling efforts. We can summarize our analysis as follows:

1. We determine dispersion profiles with better errors and higher resolution and a range covering $1''$–$300''$, reaching the half-light radius of the cluster. The dispersion profiles show a smooth behavior, with a steady increase from $0.52\,\mathrm{mas\,yr^{-1}}$ ($13.6\,\mathrm{km\,s^{-1}}$) at the half-light radius toward $\sim 0.81\,\mathrm{mas\,yr^{-1}}$ ($21.1\,\mathrm{km\,s^{-1}}$) within the 10 central arcseconds. We also study the anisotropy of the velocity dispersion field. In the inner region ($r < 30''$), the velocity distribution is isotropic; at larger radii, it starts to become increasingly radially anisotropic, reaching $\sigma_{\mathrm{PM,tan}}/\sigma_{\mathrm{PM,rad}} = 0.0849 \pm 0.003$ at the half-light radius.
2. Besides the one-dimensional profiles, we also calculate two-dimensional velocity dispersion maps. Fitting these maps with a smooth Gaussian model allows us to recover the ellipticity of the velocity field, the position angle, and the kinematic center (which is in agreement with the photometric center derived in J. Anderson & R. P. van der Marel 2010).
3. The line-of-sight velocities cover a smaller range in magnitudes but allow us to directly study the rotation curve of the cluster. At small radii ($r \leqslant 30''$), we can recover the counter-rotating signal described in R. Pechetti et al. (2024), but with lower significance, as our spectroscopic sample is limited to brighter magnitudes. Outside this region, there is a continuous increase of the rotation curve until it converges to a value of around $7\,\mathrm{km\,s^{-1}}$ at $r \approx 150''$. This is consistent with findings from the plane-of-sky rotation (M. Häberle et al. 2024a). The line-of-sight velocity dispersion profile shows a monotonic increase toward the center. A comparison with the proper-motion dispersion profile yields consistent results. By calculating the ratio between the two, we can obtain a kinematic distance estimate of (5494 ± 61) pc, the most precise kinematic distance estimate derived for ω Cen—and in good agreement with previous results in H. Baumgardt & E. Vasiliev (2021).
4. We split our sample into four metallicity quartiles and searched for variations of the kinematics with metallicity. We do not find metallicity-dependent variations in any of our velocity directions (radial proper motions, tangential proper motions, and line-of-sight velocities.). We note, however, that we have to significantly restrict the data set to a smaller subset of 6193 stars. In principle, the large number of stars with proper motions and precise photometry should enable the search for more subtle variations that were not detectable with the used subset.
5. The precise proper-motion measurements down to faint magnitudes allow us to study the state of energy equipartition of the cluster for stars with a wide range of masses ($0.288\,M_\odot$–$0.690\,M_\odot$). We measure a low degree of energy equipartition in the cluster center ($\eta = 0.088 \pm 0.017$) that decreases further toward larger radii. Interestingly, the radial component of the energy equipartition shows a much quicker decrease with radius than the tangential component, whose profile is relatively shallow.
6. Our kinematic profiles and maps are made public along with the paper in a Zenodo archive.[12] A description of the data products and tabular versions of the kinematic profiles is given in Appendix A.

The next step for a better understanding of the dynamics of ω Cen will be to fit dynamical models to the kinematic data (R. Pechetti et al. 2025, in preparation; P. Smith et al. 2025, in preparation). Our rich data set, which allowed us to accurately measure many peculiar features of ω Cen, such as rotation, flattening, anisotropy, partial energy equipartition, and fast-moving central stars, poses both a challenge and an opportunity for all future modeling efforts. While our data cover the region within the half-light radius, they can be complemented with proper-motion measurements obtained with the HST at larger distances from the cluster center (A. Bellini et al. 2018; M. Scalco et al. 2024) and data from the ESA Gaia mission (Gaia Collaboration et al. 2023); in addition, there are collections of individual radial velocities at large radii obtained with multi-object spectrographs (see H. Baumgardt & M. Hilker 2018).

Acknowledgments

We would like to thank the anonymous referee for the helpful comments, which greatly improved this work. A.C.S. acknowledges support from Hubble Space Telescope grant GO-16777. M.H. thanks Francisco Aros for useful suggestions that improved the manuscript. A.F.K. acknowledges funding from the Austrian Science Fund (FWF) [grant DOI: 10.55776/ESP542]. S.K.A. gratefully acknowledges funding from UKRI through a Future Leaders Fellowship (grant MR/Y034147/1). M.A.C. acknowledges the support from FONDECYT Postdoctorado project No. 3230727.

Software: astropy (Astropy Collaboration et al. 2022), matplotlib (J. D. Hunter 2007), numpy (C. R. Harris et al. 2020), scipy (P. Virtanen et al. 2020), IPython (F. Perez & B. E. Granger 2007), emcee (D. Foreman-Mackey et al. 2013a), VorBin (M. Cappellari & Y. Copin 2003).

Appendix A
Data Products

One of the main purposes of this work is to provide the community with a state-of-the-art kinematic analysis of the inner regions of ω Cen, using the novel oMEGACat data, that can be used to dynamically model the cluster. Therefore, we publish the following data products along with the paper. The data can be accessed using the following Zenodo archive: DOI: 10.5281/zenodo.14978551.

---

[12] DOI:10.5281/zenodo.14978551.

Table 1
Content of the Catalog and Selection File

Column	Description	Unit
`ID`	oMEGACat II Identifier; same as in Paper II (M. Häberle et al. 2024a)	⋯
`RA`	R.A. α; Paper II	degree
`DEC`	decl. δ; Paper II	degree
`x`	*x*-coordinate in pixel-based coordinate system; Paper II	40 mas ($\sim$ 1 WFC3/UVIS pixel)
`y`	*y*-coordinate in pixel-based coordinate system; Paper II	40 mas ($\sim$ 1 WFC3/UVIS pixel)
`pmra_corrected`	Locally corrected proper motion in R.A. direction; Paper II	mas yr^{-1}
`pmdec_corrected`	Locally corrected proper motion in decl. direction; Paper II	mas yr^{-1}
`pmra_corrected_err`	Error on locally corrected proper motion in R.A. direction; Paper II	mas yr^{-1}
`pmdec_corrected_err`	Error on locally corrected proper motion in decl. direction; Paper II	mas yr^{-1}
`vlos`	Line-of-sight velocity; Paper I	km s^{-1}
`vlos_err`	Error on line-of-sight velocity; Paper I	km s^{-1}
`f625w`	Magnitude in the F625W filter (diff. red. corrected); Paper II	⋯
`f814w`	Magnitude in the F814W filter (diff. red. corrected); Paper II	⋯
`nitschai_id`	ID in *oMEGACat I* MUSE spectroscopic catalog (M. S. Nitschai et al. 2023)	⋯
`voronoi_bin_ids_pm`	Attribution to Voronoi bins in proper-motion-based kinematic maps	⋯
`voronoi_bin_ids_los`	Attribution to Voronoi bins in line-of-sight-based kinematic maps	⋯
`selection_hq_f625w`	High-quality flag for F625W photometry	⋯
`selection_hq_f814w`	High-quality flag for F814W photometry	⋯
`selection_hq_astrometry`	High-quality flag for astrometry	⋯
`selection_hq_astrometry_and_membership`	Combined criteria for proper-motion quality and cluster membership (CMD and vector-point diagram selections). This is the sample used for the proper-motion-based analysis.	⋯
`selection_hq_los`	High-quality flag for line-of-sight velocity measurements	⋯
`selection_hq_pm_and_los`	Combined proper motion and line-of-sight velocity flag. This is the sample used for the analysis based on line-of-sight velocity.	⋯

All files are provided both as fits tables (file ending: $*$.fits) and as machine-readable text files (file ending: $*$.dat). The following files are contained in the archive:

1. IPython Notebook containing examples on how to read and plot the different data products
   - (a) `data_products_demonstration_and_test.ipynb`
2. A set of selections that can be applied to the catalog in order to obtain the high-quality subsample that we have used for our analysis:
   - (a) `catalog_and_selections.fits` This file contains the selections, and for convenience, also includes various other columns taken from the oMEGACat catalogs. A description of the content is given in Table 1.
3. Proper-motion dispersion profiles (combined, radial, and tangential) using different binning schemes
   - (a) Adaptive logarithmic bins: `proper_motion_dispersion_log_bins.fits` (see also Table 2)
   - (b) Linear bins: `proper_motion_dispersion_lin_bins.fits`
   - (c) Equal-number bins: `proper_motion_dispersion_equaln_bins.fits`
4. LOS profiles (rotation, dispersion, and position angle)
   - (a) `los_profile.fits` (see also Table 3)
5. Kinematic maps
   - (a) Proper-motion dispersion measurements: `proper_motion_dispersion_voronoi_bins.fits`
   - (b) Line-of-sight mean velocity and dispersion measurements: `los_dispersion_and_rotation_voronoi_bins.fits`
6. Data to reproduce the energy equipartition experiments
   - (a) Velocity dispersion profiles split into nine equally populated mass bins: `energy_equipartition_profiles.fits`

Table 2
Tabular Version of Proper-motion Dispersion Profile

$r_{\rm lower}$ (arcsec)	$r_{\rm median}$ (arcsec)	$r_{\rm upper}$ (arcsec)	$N_{\rm Stars}$ ⋯	$\sigma_{\rm PM,c}$ (mas yr^{-1})	$\sigma_{\rm PM,rad}$ (mas yr^{-1})	$\sigma_{\rm PM,tan}$ (mas yr^{-1})	$\sigma_{\rm PM,c}$ (km s^{-1})	$\sigma_{\rm PM,rad}$ (km s^{-1})	$\sigma_{\rm PM,tan}$ (km s^{-1})	Anisotropy $\sigma_{\rm rad}/\sigma_{\rm tan}$ ⋯
0.00	1.82	2.68	100	$0.793^{+0.038}_{-0.037}$	$0.840^{+0.060}_{-0.062}$	$0.755^{+0.059}_{-0.048}$	$20.67^{+1.00}_{-0.96}$	$21.89^{+1.56}_{-1.61}$	$19.68^{+1.53}_{-1.24}$	0.899±0.091
2.68	3.33	3.78	100	$0.812^{+0.041}_{-0.040}$	$0.813^{+0.060}_{-0.060}$	$0.841^{+0.066}_{-0.050}$	$21.15^{+1.07}_{-1.04}$	$21.18^{+1.57}_{-1.55}$	$21.93^{+1.71}_{-1.30}$	1.035±0.104
3.78	4.24	4.67	101	$0.798^{+0.042}_{-0.037}$	$0.818^{+0.059}_{-0.054}$	$0.792^{+0.055}_{-0.050}$	$20.79^{+1.09}_{-0.96}$	$21.30^{+1.54}_{-1.41}$	$20.63^{+1.44}_{-1.31}$	0.969±0.093
4.67	5.00	5.34	101	$0.885^{+0.051}_{-0.039}$	$0.856^{+0.066}_{-0.053}$	$0.925^{+0.079}_{-0.070}$	$23.06^{+1.33}_{-1.02}$	$22.31^{+1.73}_{-1.39}$	$24.09^{+2.05}_{-1.83}$	1.080±0.115
5.34	5.66	5.99	109	$0.851^{+0.036}_{-0.043}$	$0.894^{+0.063}_{-0.060}$	$0.820^{+0.058}_{-0.049}$	$22.18^{+0.95}_{-1.12}$	$23.29^{+1.64}_{-1.56}$	$21.37^{+1.51}_{-1.28}$	0.917±0.087
5.99	6.36	6.72	137	$0.832^{+0.040}_{-0.036}$	$0.821^{+0.055}_{-0.048}$	$0.836^{+0.049}_{-0.044}$	$21.69^{+1.03}_{-0.94}$	$21.40^{+1.43}_{-1.26}$	$21.80^{+1.27}_{-1.15}$	1.018±0.085

Table 2
(Continued)

r_{lower} (arcsec)	r_{median} (arcsec)	r_{upper} (arcsec)	N_{Stars} ⋯	$\sigma_{\text{PM,c}}$ (mas yr^{-1})	$\sigma_{\text{PM,rad}}$ (mas yr^{-1})	$\sigma_{\text{PM,tan}}$ (mas yr^{-1})	$\sigma_{\text{PM,c}}$ (km s^{-1})	$\sigma_{\text{PM,rad}}$ (km s^{-1})	$\sigma_{\text{PM,tan}}$ (km s^{-1})	Anisotropy $\sigma_{\text{rad}}/\sigma_{\text{tan}}$ ⋯
6.72	7.13	7.54	147	$0.768^{+0.032}_{-0.026}$	$0.800^{+0.046}_{-0.045}$	$0.734^{+0.053}_{-0.040}$	$20.01^{+0.82}_{-0.69}$	$20.84^{+1.21}_{-1.17}$	$19.14^{+1.39}_{-1.03}$	0.918±0.078
7.54	8.00	8.46	204	$0.792^{+0.028}_{-0.031}$	$0.747^{+0.036}_{-0.037}$	$0.830^{+0.044}_{-0.041}$	$20.63^{+0.73}_{-0.80}$	$19.46^{+0.94}_{-0.97}$	$21.63^{+1.15}_{-1.08}$	1.112±0.079
8.46	9.05	9.50	227	$0.769^{+0.024}_{-0.025}$	$0.775^{+0.036}_{-0.036}$	$0.763^{+0.042}_{-0.032}$	$20.04^{+0.63}_{-0.64}$	$20.20^{+0.94}_{-0.94}$	$19.88^{+1.09}_{-0.83}$	0.984±0.066
9.50	10.04	10.65	271	$0.796^{+0.023}_{-0.021}$	$0.799^{+0.043}_{-0.034}$	$0.796^{+0.037}_{-0.036}$	$20.74^{+0.59}_{-0.56}$	$20.82^{+1.13}_{-0.89}$	$20.75^{+0.95}_{-0.94}$	0.997±0.066
10.65	11.29	11.95	363	$0.763^{+0.019}_{-0.020}$	$0.794^{+0.032}_{-0.029}$	$0.738^{+0.030}_{-0.026}$	$19.90^{+0.51}_{-0.51}$	$20.69^{+0.83}_{-0.76}$	$19.22^{+0.78}_{-0.68}$	0.929±0.050
11.95	12.70	13.41	419	$0.767^{+0.020}_{-0.018}$	$0.757^{+0.026}_{-0.021}$	$0.779^{+0.030}_{-0.026}$	$20.00^{+0.53}_{-0.46}$	$19.72^{+0.69}_{-0.55}$	$20.29^{+0.77}_{-0.68}$	1.029±0.049
13.41	14.26	15.05	540	$0.775^{+0.016}_{-0.016}$	$0.795^{+0.024}_{-0.026}$	$0.768^{+0.024}_{-0.020}$	$20.20^{+0.43}_{-0.43}$	$20.71^{+0.63}_{-0.68}$	$20.01^{+0.64}_{-0.53}$	0.966±0.041
15.05	16.00	16.88	720	$0.775^{+0.015}_{-0.013}$	$0.789^{+0.022}_{-0.020}$	$0.764^{+0.017}_{-0.022}$	$20.20^{+0.40}_{-0.35}$	$20.56^{+0.57}_{-0.52}$	$19.92^{+0.44}_{-0.58}$	0.969±0.036
16.88	18.03	18.94	821	$0.778^{+0.015}_{-0.013}$	$0.789^{+0.018}_{-0.017}$	$0.766^{+0.018}_{-0.017}$	$20.26^{+0.38}_{-0.34}$	$20.57^{+0.48}_{-0.45}$	$19.97^{+0.46}_{-0.45}$	0.971±0.031
18.94	20.16	21.25	1099	$0.776^{+0.012}_{-0.011}$	$0.783^{+0.015}_{-0.017}$	$0.769^{+0.016}_{-0.014}$	$20.23^{+0.30}_{-0.29}$	$20.41^{+0.39}_{-0.43}$	$20.05^{+0.41}_{-0.36}$	0.982±0.027
21.25	22.62	23.85	1426	$0.756^{+0.010}_{-0.009}$	$0.763^{+0.015}_{-0.016}$	$0.750^{+0.014}_{-0.015}$	$19.70^{+0.25}_{-0.23}$	$19.87^{+0.40}_{-0.41}$	$19.54^{+0.36}_{-0.39}$	0.983±0.028
23.85	25.28	26.76	1779	$0.767^{+0.010}_{-0.009}$	$0.771^{+0.013}_{-0.012}$	$0.764^{+0.013}_{-0.012}$	$19.99^{+0.25}_{-0.24}$	$20.10^{+0.34}_{-0.31}$	$19.91^{+0.33}_{-0.33}$	0.990±0.023
26.76	28.43	30.02	2299	$0.748^{+0.008}_{-0.007}$	$0.738^{+0.013}_{-0.010}$	$0.757^{+0.012}_{-0.011}$	$19.50^{+0.20}_{-0.18}$	$19.22^{+0.34}_{-0.26}$	$19.72^{+0.30}_{-0.28}$	1.026±0.022
30.02	31.95	33.68	2912	$0.764^{+0.008}_{-0.007}$	$0.761^{+0.011}_{-0.009}$	$0.767^{+0.011}_{-0.009}$	$19.90^{+0.21}_{-0.18}$	$19.82^{+0.29}_{-0.24}$	$19.98^{+0.28}_{-0.24}$	1.008±0.019
33.68	35.81	37.79	3587	$0.758^{+0.006}_{-0.006}$	$0.754^{+0.008}_{-0.009}$	$0.765^{+0.008}_{-0.010}$	$19.75^{+0.17}_{-0.15}$	$19.65^{+0.20}_{-0.24}$	$19.93^{+0.22}_{-0.26}$	1.014±0.017
37.79	40.17	42.40	4709	$0.741^{+0.005}_{-0.005}$	$0.745^{+0.009}_{-0.008}$	$0.736^{+0.008}_{-0.007}$	$19.31^{+0.13}_{-0.14}$	$19.40^{+0.24}_{-0.21}$	$19.18^{+0.22}_{-0.17}$	0.989±0.015
42.40	45.04	47.58	5591	$0.737^{+0.005}_{-0.005}$	$0.744^{+0.006}_{-0.008}$	$0.732^{+0.008}_{-0.007}$	$19.21^{+0.14}_{-0.12}$	$19.40^{+0.17}_{-0.20}$	$19.07^{+0.20}_{-0.17}$	0.983±0.013
47.58	50.58	53.38	6940	$0.740^{+0.005}_{-0.004}$	$0.745^{+0.006}_{-0.006}$	$0.735^{+0.006}_{-0.006}$	$19.28^{+0.12}_{-0.11}$	$19.42^{+0.16}_{-0.16}$	$19.14^{+0.16}_{-0.16}$	0.986±0.012
53.38	56.70	59.89	9066	$0.735^{+0.004}_{-0.003}$	$0.740^{+0.005}_{-0.005}$	$0.732^{+0.006}_{-0.006}$	$19.15^{+0.11}_{-0.09}$	$19.29^{+0.14}_{-0.14}$	$19.07^{+0.15}_{-0.15}$	0.988±0.010
59.89	63.58	67.20	10920	$0.725^{+0.003}_{-0.003}$	$0.731^{+0.005}_{-0.005}$	$0.719^{+0.005}_{-0.005}$	$18.90^{+0.09}_{-0.09}$	$19.04^{+0.13}_{-0.14}$	$18.75^{+0.14}_{-0.12}$	0.985±0.010
67.20	71.42	75.40	13445	$0.724^{+0.003}_{-0.003}$	$0.728^{+0.004}_{-0.005}$	$0.720^{+0.004}_{-0.004}$	$18.87^{+0.07}_{-0.08}$	$18.96^{+0.11}_{-0.12}$	$18.76^{+0.10}_{-0.11}$	0.990±0.008
75.40	80.09	84.60	16942	$0.712^{+0.003}_{-0.002}$	$0.721^{+0.003}_{-0.004}$	$0.704^{+0.004}_{-0.004}$	$18.56^{+0.07}_{-0.06}$	$18.80^{+0.09}_{-0.10}$	$18.34^{+0.10}_{-0.10}$	0.975±0.007
84.60	89.93	94.93	20309	$0.705^{+0.002}_{-0.003}$	$0.711^{+0.003}_{-0.003}$	$0.698^{+0.003}_{-0.003}$	$18.37^{+0.06}_{-0.07}$	$18.54^{+0.08}_{-0.08}$	$18.18^{+0.09}_{-0.08}$	0.981±0.006
94.93	100.73	106.51	23917	$0.692^{+0.002}_{-0.002}$	$0.702^{+0.003}_{-0.003}$	$0.681^{+0.003}_{-0.003}$	$18.02^{+0.05}_{-0.06}$	$18.29^{+0.08}_{-0.08}$	$17.75^{+0.07}_{-0.08}$	0.971±0.006
106.51	112.97	119.50	27379	$0.682^{+0.002}_{-0.002}$	$0.694^{+0.003}_{-0.003}$	$0.671^{+0.003}_{-0.002}$	$17.76^{+0.06}_{-0.04}$	$18.08^{+0.08}_{-0.08}$	$17.48^{+0.07}_{-0.06}$	0.967±0.006
119.50	126.76	134.09	30196	$0.669^{+0.002}_{-0.002}$	$0.686^{+0.003}_{-0.003}$	$0.652^{+0.003}_{-0.003}$	$17.44^{+0.05}_{-0.05}$	$17.86^{+0.07}_{-0.07}$	$17.00^{+0.07}_{-0.07}$	0.952±0.005
134.09	142.43	150.45	34236	$0.655^{+0.002}_{-0.002}$	$0.678^{+0.003}_{-0.002}$	$0.629^{+0.003}_{-0.002}$	$17.06^{+0.04}_{-0.05}$	$17.68^{+0.07}_{-0.06}$	$16.40^{+0.07}_{-0.06}$	0.928±0.005
150.45	160.11	168.80	43889	$0.636^{+0.001}_{-0.001}$	$0.662^{+0.002}_{-0.002}$	$0.610^{+0.002}_{-0.002}$	$16.58^{+0.04}_{-0.04}$	$17.25^{+0.06}_{-0.06}$	$15.89^{+0.06}_{-0.05}$	0.921±0.004
168.80	179.11	189.40	54408	$0.621^{+0.001}_{-0.001}$	$0.647^{+0.002}_{-0.002}$	$0.593^{+0.002}_{-0.002}$	$16.18^{+0.04}_{-0.03}$	$16.86^{+0.05}_{-0.06}$	$15.46^{+0.05}_{-0.04}$	0.917±0.004
189.40	201.15	212.51	61707	$0.601^{+0.001}_{-0.001}$	$0.634^{+0.002}_{-0.002}$	$0.565^{+0.002}_{-0.002}$	$15.65^{+0.03}_{-0.03}$	$16.51^{+0.05}_{-0.04}$	$14.73^{+0.05}_{-0.04}$	0.892±0.004
212.51	225.54	238.44	71611	$0.584^{+0.001}_{-0.001}$	$0.619^{+0.002}_{-0.002}$	$0.546^{+0.001}_{-0.002}$	$15.21^{+0.03}_{-0.03}$	$16.13^{+0.04}_{-0.04}$	$14.23^{+0.04}_{-0.04}$	0.882±0.003
238.44	252.36	267.54	78997	$0.562^{+0.001}_{-0.001}$	$0.602^{+0.002}_{-0.002}$	$0.519^{+0.001}_{-0.001}$	$14.63^{+0.02}_{-0.03}$	$15.68^{+0.04}_{-0.04}$	$13.52^{+0.04}_{-0.03}$	0.862±0.003
267.54	280.94	300.18	60637	$0.544^{+0.001}_{-0.001}$	$0.586^{+0.002}_{-0.001}$	$0.497^{+0.001}_{-0.001}$	$14.17^{+0.03}_{-0.03}$	$15.26^{+0.05}_{-0.04}$	$12.96^{+0.03}_{-0.04}$	0.849±0.003
300.18	311.12	346.07	18485	$0.520^{+0.002}_{-0.002}$	$0.562^{+0.003}_{-0.003}$	$0.474^{+0.003}_{-0.002}$	$13.54^{+0.05}_{-0.05}$	$14.66^{+0.07}_{-0.08}$	$12.36^{+0.07}_{-0.06}$	0.843±0.006

Note. We also show physical velocity values, converted using our kinematic distance estimate of 5494 pc.

Table 3
Tabular Version of LOS Dispersion Profile

r_{lower} (arcsec)	r_{median} (arcsec)	r_{upper} (arcsec)	N_{Stars} ⋯	v_{LOS} (km s^{-1})	σ_{LOS} (km s^{-1})	θ_0 (deg)
0.00	5.66	7.90	50	$10.3^{+5.1}_{-4.8}$	$20.9^{+2.5}_{-1.9}$	$-135.8^{+21.2}_{-20.9}$
7.90	9.41	11.35	50	$4.7^{+3.3}_{-3.9}$	$19.0^{+2.1}_{-2.0}$	$-169.7^{+50.5}_{-46.4}$
11.35	13.41	14.51	50	$8.3^{+4.0}_{-4.0}$	$21.0^{+2.3}_{-1.9}$	$175.6^{+26.9}_{-32.4}$
14.51	16.09	17.08	51	$10.0^{+4.4}_{-4.7}$	$20.4^{+2.6}_{-1.7}$	$41.2^{+21.7}_{-23.9}$
17.08	18.68	19.68	51	$8.2^{+3.9}_{-3.7}$	$17.9^{+1.8}_{-1.7}$	$116.9^{+24.4}_{-29.1}$
19.68	20.91	22.09	64	$5.9^{+2.9}_{-3.3}$	$18.0^{+1.7}_{-1.6}$	$74.6^{+35.2}_{-32.6}$
22.09	23.55	24.78	92	$0.8^{+2.6}_{-3.1}$	$20.9^{+2.1}_{-1.7}$	$-12.1^{+99.1}_{-113.5}$
24.78	26.31	27.79	137	$3.1^{+2.9}_{-2.5}$	$21.4^{+1.5}_{-1.3}$	$36.9^{+45.3}_{-50.7}$
27.79	29.52	31.17	119	$3.2^{+2.4}_{-2.5}$	$18.4^{+1.4}_{-1.2}$	$79.5^{+42.9}_{-37.9}$
31.17	33.24	34.98	179	$1.6^{+2.0}_{-1.9}$	$18.4^{+0.9}_{-0.8}$	$-128.4^{+59.4}_{-72.9}$
34.98	37.15	39.26	224	$4.6^{+1.9}_{-1.4}$	$18.3^{+0.9}_{-0.9}$	$116.4^{+20.7}_{-21.8}$
39.26	41.55	44.05	282	$2.5^{+1.5}_{-1.4}$	$19.1^{+0.9}_{-0.8}$	$73.8^{+37.1}_{-38.4}$
44.05	46.97	49.43	359	$3.8^{+1.2}_{-1.4}$	$18.6^{+0.6}_{-0.6}$	$101.7^{+25.0}_{-21.7}$

Table 3
(Continued)

r_{lower} (arcsec)	r_{median} (arcsec)	r_{upper} (arcsec)	N_{Stars} ⋯	v_{LOS} (km s^{-1})	σ_{LOS} (km s^{-1})	θ_0 (deg)
49.43	52.60	55.47	457	$3.9^{+1.2}_{-1.1}$	$17.6^{+0.5}_{-0.6}$	$122.4^{+16.1}_{-16.5}$
55.47	58.79	62.26	590	$2.6^{+1.0}_{-1.2}$	$19.6^{+0.6}_{-0.6}$	$71.0^{+26.2}_{-27.7}$
62.26	66.08	69.86	591	$4.4^{+1.0}_{-1.0}$	$18.4^{+0.6}_{-0.6}$	$115.8^{+12.6}_{-16.5}$
69.86	74.29	78.39	766	$4.3^{+0.9}_{-0.8}$	$18.4^{+0.5}_{-0.5}$	$86.1^{+13.2}_{-12.5}$
78.39	83.43	87.95	903	$4.4^{+0.8}_{-0.8}$	$18.8^{+0.5}_{-0.4}$	$92.1^{+11.3}_{-14.7}$
87.95	93.34	98.68	1107	$4.3^{+0.7}_{-0.7}$	$17.2^{+0.4}_{-0.3}$	$99.5^{+9.4}_{-11.4}$
98.68	104.57	110.72	1291	$5.0^{+0.7}_{-0.8}$	$17.8^{+0.3}_{-0.4}$	$107.6^{+8.1}_{-8.8}$
110.72	117.26	124.24	1239	$4.8^{+0.8}_{-0.7}$	$17.1^{+0.3}_{-0.3}$	$92.1^{+8.5}_{-9.5}$
124.24	131.59	139.40	1274	$5.4^{+0.6}_{-0.7}$	$17.3^{+0.4}_{-0.4}$	$94.8^{+7.4}_{-7.3}$
139.40	148.36	156.42	1755	$6.6^{+0.5}_{-0.4}$	$16.4^{+0.3}_{-0.3}$	$98.3^{+5.4}_{-5.1}$
156.42	166.17	175.50	2098	$6.8^{+0.5}_{-0.5}$	$15.9^{+0.2}_{-0.2}$	$110.0^{+4.3}_{-4.6}$
175.50	186.00	196.92	2358	$7.0^{+0.5}_{-0.5}$	$15.5^{+0.2}_{-0.3}$	$109.4^{+3.4}_{-3.5}$
196.92	208.94	220.95	2453	$6.4^{+0.4}_{-0.4}$	$14.6^{+0.2}_{-0.2}$	$100.9^{+4.0}_{-3.6}$
220.95	234.05	247.90	2662	$6.1^{+0.4}_{-0.4}$	$14.2^{+0.2}_{-0.2}$	$103.4^{+3.9}_{-4.0}$
247.90	261.11	278.14	2401	$6.6^{+0.3}_{-0.3}$	$13.7^{+0.2}_{-0.2}$	$105.9^{+3.8}_{-3.7}$
278.14	290.28	332.28	1275	$6.6^{+0.5}_{-0.4}$	$12.5^{+0.2}_{-0.3}$	$106.8^{+5.4}_{-4.1}$

Table 4
Comparison of Our New Kinematic Distance Estimates with Various Recent Literature Estimates

Distance	Data and Method	Reference
(5494 ± 61) pc	oMEGACat, kin. dist.	This work
(5240±110) pc	Gaia EDR3, parallax	J. Soltis et al. (2021)
($5485^{+0.302}_{-0.272}$) pc	Gaia EDR3, parallax	H. Baumgardt & E. Vasiliev (2021)
(5359±141) pc	Gaia EDR3, kin. dist.	H. Baumgardt & E. Vasiliev (2021)
(5264±121) pc	HST, kin. dist.	H. Baumgardt & E. Vasiliev (2021)

(b) A table containing information of the mean mass in each bin: `energy_equipartition_massbins.fits`

Appendix B
Plots Describing the Selections

Several cuts in astrometric and photometric quality parameters were used to restrict the full oMEGACat II catalog to a subsample of reliable proper-motion measurements (see also Section 2). Figure 18 shows the overall distributions and thresholds for the parameters used for the astrometric selection. Figure 19 shows magnitude-dependent photometric quantities (e.g., the QFIT parameter and the relative flux values of neighboring sources) as well as the spatial distribution of photometrically well-measured sources.

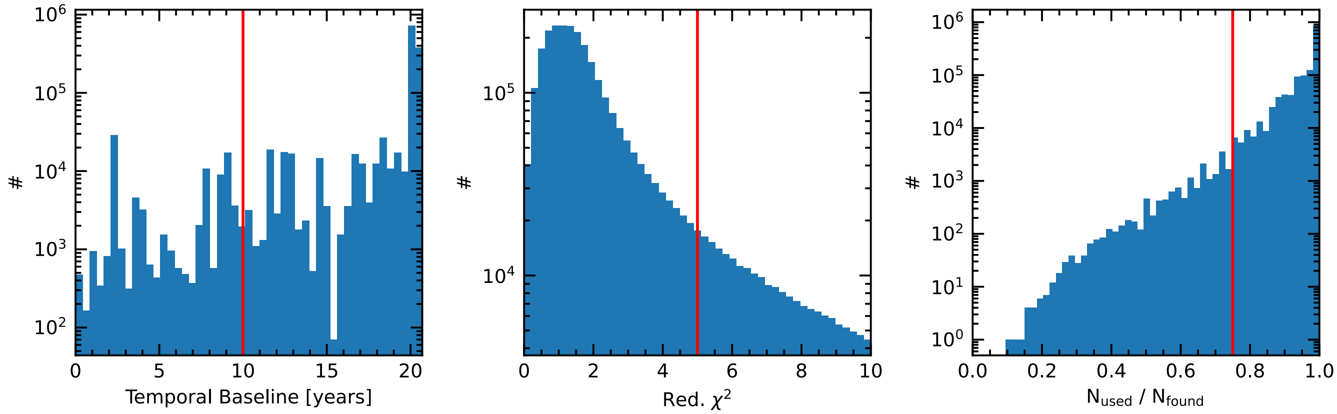

Figure 18. Histograms and thresholds of the astrometric quality parameters used to define the high-quality subsample of reliable proper-motion measurements. Left: Temporal baseline used for proper-motion determination, Center: Reduced χ^2 value of the linear fit to the astrometric data used to determine the proper motions. Right: Fraction of measurements used for the proper-motion fit. A low value indicates unreliable astrometry.

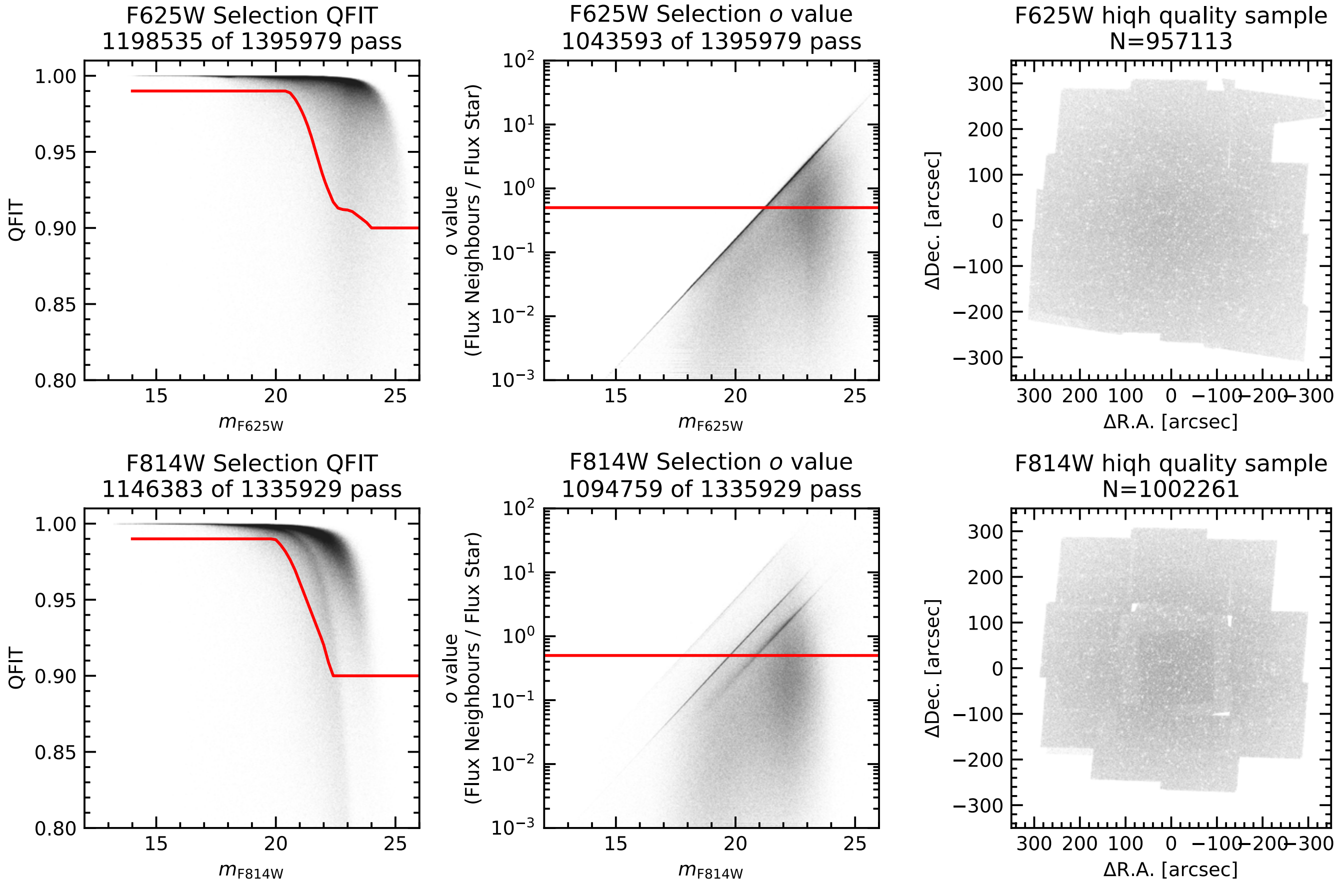

Figure 19. Photometric quality selections used to determine a high-quality subset of the data for both the ACS WFC F625W filter (top) and the WFC3/UVIS F814W filter (bottom). Left: Magnitude-dependent threshold on the QFIT value that characterizes how well the point-spread function could be fit to the data. Center: *o* value that characterized the fraction of flux from neighboring sources for each photometric measurement. Right: Spatial distribution of well-measured stars. The measurements in the F625W are quite uniformly distributed. The F814W measurements show some spatial dependences and minor gaps, due to the distribution of pointings.

Appendix C
Comparison of Kinematic Distance Estimates

Our new kinematic distance estimate for ω Cen is $d = (5494 \pm 61)$ pc. In Table 4, we compare it with several other recent distance estimates, for which there is overall good agreement. We refer to H. Baumgardt & E. Vasiliev (2021) for a more extensive discussion of previous distance measurements to ω Cen.

Appendix D
Variation of Binning Schemes

D.1. Radii of Circular Bins

Traditionally, the velocity dispersion has been measured in circular radial bins. The choice of the bin radii is ultimately arbitrary, and with more than 600,000 individual stellar measurements and a large radial range of around 350″, several binning schemes are feasible. In Figure 20, we explore three different binning options: our first binning choice is an adaptive, logarithmic binning scheme. The step size is $\Delta \log r = 0.05$, but we require a minimum number of at least 100 stars per bin. This binning choice has a high resolution in the centermost region while being more coarse in the outer regions. The second binning scheme explored is a simple linear scheme with a bin size of $\Delta r = 2''.5$, naturally maintaining a uniform resolution in both the inner and outer regions. Finally, we explored equally populated bins with a number of $N = 250$ stars per bin. The advantage of this scheme is the uniform uncertainties in all bins. However, the resolution in the center is comparatively low, while the bin density is very large at larger radii. The three binning schemes agree with each other within their uncertainties and we make all profiles publicly available, so that the user can choose the scheme most appropriate to their science case. For our further discussions, we use the first adaptive logarithmic binning scheme.

D.2. Testing Elliptical Instead of Circular Bins

The stellar density and the surface brightness of ω Cen show significant flattening with variable ellipticity that reaches a maximum of $\epsilon = 1 - \frac{b}{a} = 0.16$ at $r = 8'$ and a mean value of $\epsilon = 0.10$ (E. H. Geyer et al. 1983; E. Pancino et al. 2003; A. Calamida et al. 2020). Therefore, the choice of circular bins might not fully capture the nature of the dispersion profile of the cluster. To determine the ellipticity of the 2D velocity dispersion field, we first calculated a dispersion map on a regular grid with a bin size of $5'' \times 5''$. We then symmetrized the map using the photometric J. Anderson & R. P. van der Marel (2010) center as a pivot point to fill in the gaps in the data set (see Figure 21, left). Then we used the `photutils.isophot` function to fit elliptical "isophots" (or isodispersion contours) to the map. At smaller radii ($r \leqslant 2'$), the ellipticity and position angle are poorly constrained and show large scatter. At larger radii, the ellipticity converges to a median value of $\epsilon_{\mathrm{disp.}} = 0.12$ with a median position angle of PA $= 108°$, in good agreement with the light distribution and the results of the Gaussian fits (see Figure 10). Using these values, we calculated the dispersion profile using elliptical bins instead of circular bins, but did not find significant differences when comparing bins with the same mean radii.

D.3. Variation of 2D Binning Schemes

D.3.1. Variation of the Target Number of Stars in Voronoi Bins

Our main kinematic maps (see Figure 9) were determined using a Voronoi binning scheme with a target number of $N = 250$ stars per bin. In Figure 22, we also show kinematic maps with $N = 1000$ and $N = 100$. This comparison demonstrates that $N = 250$ is a good compromise between spatial resolution and noise in the individual bins. With $N = 1000$, the variation due to stochastic noise is lower than the spatial variation, meaning that information is lost due to the large bin size. With $N = 100$, the stochastic noise starts to dominate, meaning that no further information is retained by a finer bin size.

D.3.2. Comparison between Voronoi Binning and Nearest-neighbor Schemes

The employed Voronoi binning schemes offer the advantage of splitting the data into fully independent bins that each contain a similar number of stars—and therefore yield a similar statistical noise level. Another commonly used method (see, e.g., R. Pechetti et al. 2024; M. S. Nitschai et al. 2024) to derive 2D binned maps in stellar fields is to use a nearest-neighbor scheme to group the stars. In Figure 23, we used this scheme to create a kinematic map with the same properties as

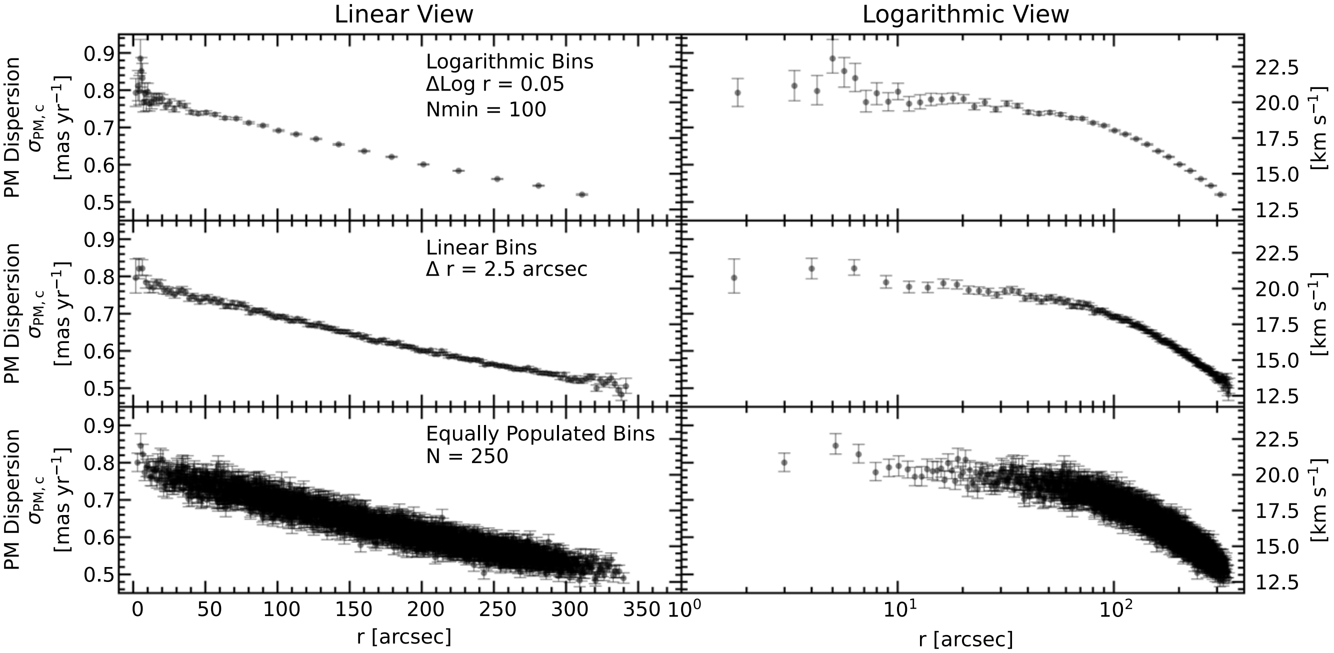

Figure 20. Comparison of the total proper-motion dispersion profile determined with various binning schemes (top: adaptive logarithmic, middle: linear/equal radius, bottom: equi-populated). The profiles are shown in both linear (left) and logarithmic (right) scale. The different profiles show overall agreement, but differ in resolution and scatter.

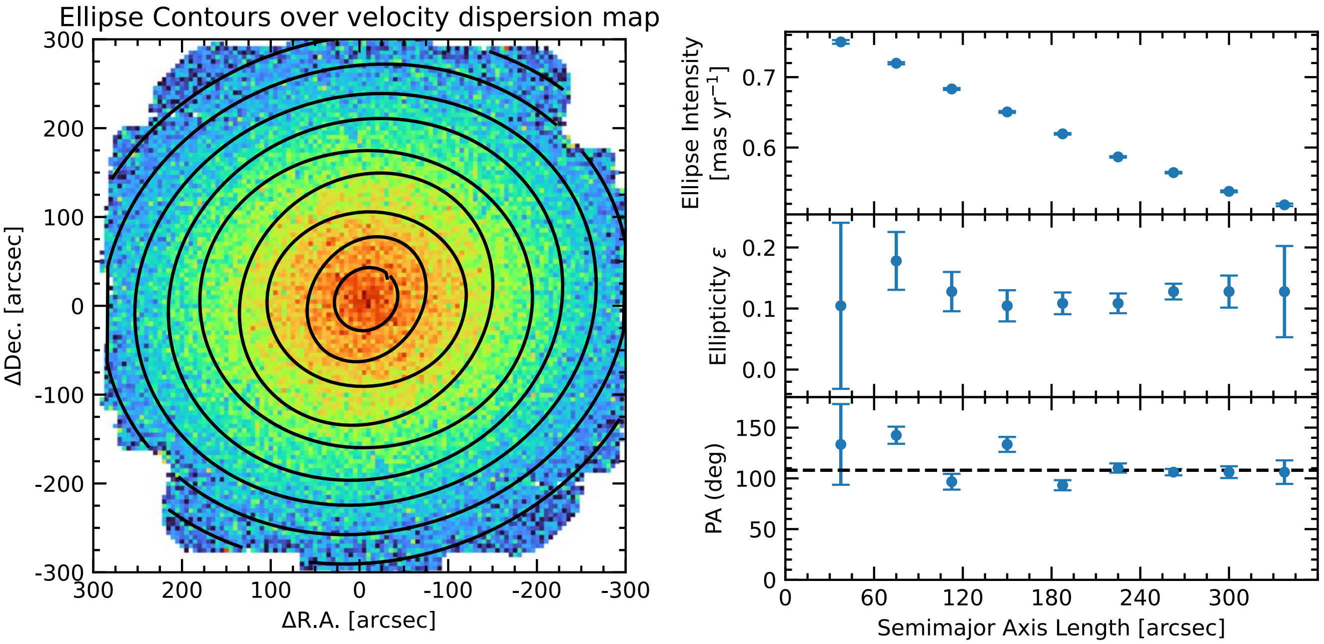

Figure 21. Determination of the ellipticity of the velocity field. Left: A symmetrized map of the proper-motion dispersion determined in 5″ × 5″ grid cells. The black ellipses show the isodispersion contours fit with `photutils.isophote`. Right: Profiles of the determined ellipse parameters of the isodispersion contours (top: dispersion, middle: ellipticity, bottom: position angle). The median ellipticity is $\epsilon_{\mathrm{disp.}} = 0.12$, and the position angle PA = 108°.

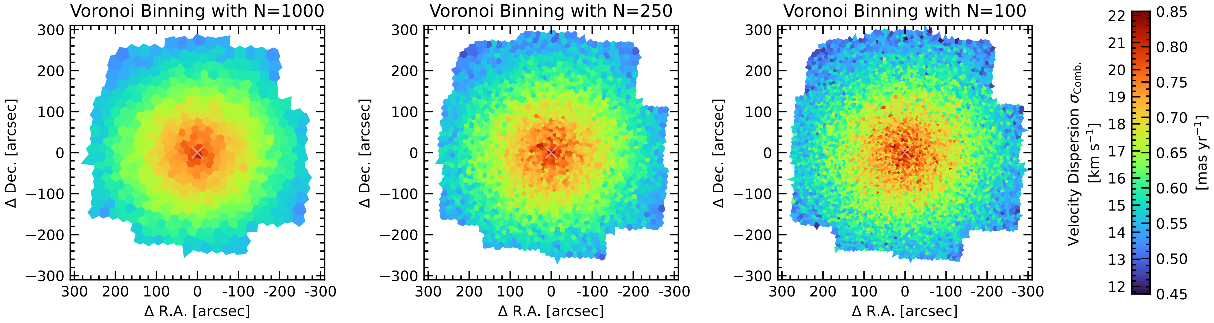

Figure 22. Comparison of proper-motion dispersion maps using three different Voronoi binning schemes with a different number of measurements per bin. Left: $N = 1000$. Center: N = 250. Right: $N = 100$.

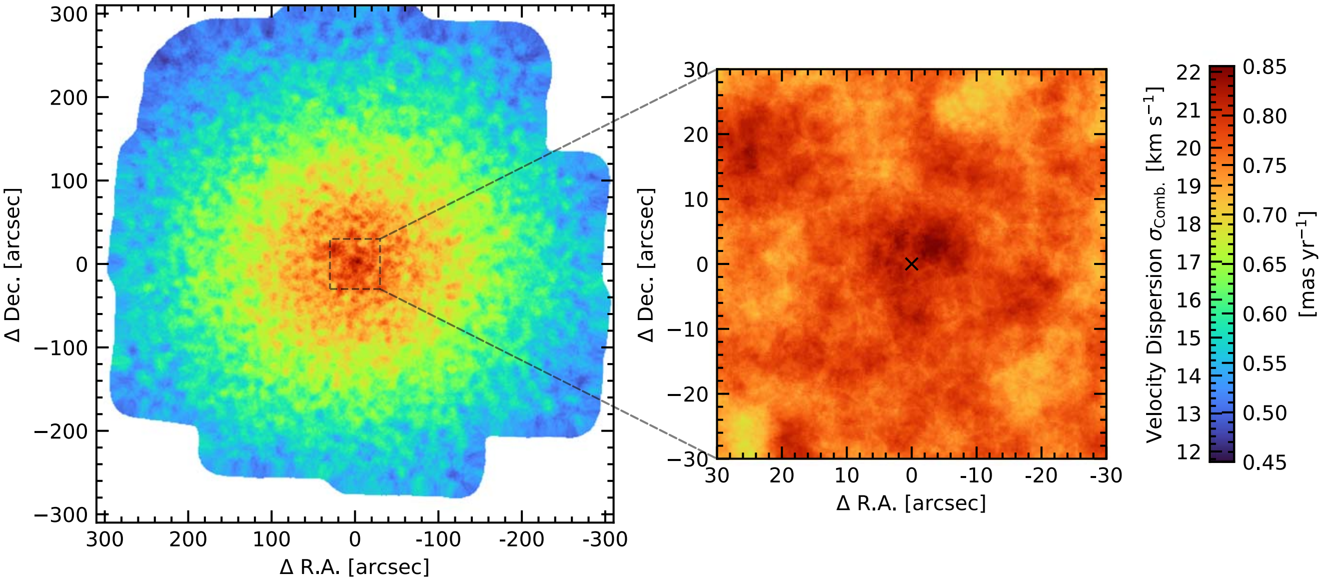

Figure 23. A proper-motion dispersion map based on a nearest-neighbor binning scheme with $N = 250$. This figure allows the KNN scheme to be compared with the Voronoi binning scheme used in Figure 9.

in Figure 9. Overall, there is good agreement between the two spatial binning methods. The KNN map shows granularity with a feature size comparable to the size of the Voronoi bins in Figure 9, which is set by the search radius necessary to find the required number of neighbors. At small scales, the KNN map has a smoother appearance (as neighboring points share a large part of their star sample). However, this should not be mistaken as better precision; it just means that the uncertainties are correlated on scales smaller than the neighbor search radius.

ORCID iDs

Maximilian Häberle https://orcid.org/0000-0002-5844-4443
N. Neumayer https://orcid.org/0000-0002-6922-2598
C. Clontz https://orcid.org/0009-0005-8057-0031
A. C. Seth https://orcid.org/0000-0003-0248-5470
P. J. Smith https://orcid.org/0000-0002-7489-5244
S. Kamann https://orcid.org/0000-0001-6604-0505
R. Pechetti https://orcid.org/0000-0002-1670-0808
M. S. Nitschai https://orcid.org/0000-0002-2941-4480
M. Alfaro-Cuello https://orcid.org/0000-0002-1212-2844
H. Baumgardt https://orcid.org/0000-0002-1959-6946
A. Bellini https://orcid.org/0000-0003-3858-637X
A. Feldmeier-Krause https://orcid.org/0000-0002-0160-7221
N. Kacharov https://orcid.org/0000-0002-6072-6669
M. Libralato https://orcid.org/0000-0001-9673-7397
A. P. Milone https://orcid.org/0000-0001-7506-930X
S. O. Souza https://orcid.org/0000-0001-8052-969X
G. van de Ven https://orcid.org/0000-0003-4546-7731
Z. Wang (王梓先) https://orcid.org/0000-0003-2512-6892

References

Alfaro-Cuello, M., Kacharov, N., Neumayer, N., et al. 2019, ApJ, 886, 57
Alfaro-Cuello, M., Kacharov, N., Neumayer, N., et al. 2020, ApJ, 892, 20
Anderson, A. J. 1997, PhD thesis, Uni. California, Berkeley, CA
Anderson, J., & van der Marel, R. P. 2010, ApJ, 710, 1032
Aros, F. I., & Vesperini, E. 2023, MNRAS, 525, 3136
Astropy Collaboration, Price-Whelan, A. M., Lim, P. L., et al. 2022, ApJ, 935, 167
Bañares-Hernández, A., Calore, F., Martin Camalich, J., & Read, J. I. 2025, A&A, 693, A104
Bacon, R., Accardo, M., Adjali, L., et al. 2010, Proc. SPIE, 7735, 773508
Baldwin, A. T., Watkins, L. L., van der Marel, R. P., et al. 2016, ApJ, 827, 12
Baumgardt, H., & Hilker, M. 2018, MNRAS, 478, 1520
Baumgardt, H., & Makino, J. 2003, MNRAS, 340, 227
Baumgardt, H., & Vasiliev, E. 2021, MNRAS, 505, 5957
Baumgardt, H., He, C., Sweet, S. M., et al. 2019, MNRAS, 488, 5340
Bedin, L. R., Piotto, G., Anderson, J., et al. 2004, ApJL, 605, L125
Bekki, K., & Freeman, K. C. 2003, MNRAS, 346, L11
Bellini, A., Anderson, J., Bedin, L. R., et al. 2017a, ApJ, 842, 6
Bellini, A., Anderson, J., van der Marel, R. P., et al. 2014, ApJ, 797, 115
Bellini, A., Bedin, L. R., Piotto, G., et al. 2010, AJ, 140, 631
Bellini, A., Milone, A. P., Anderson, J., et al. 2017b, ApJ, 844, 164
Bellini, A., Piotto, G., Bedin, L. R., et al. 2009, A&A, 507, 1393
Bellini, A., Libralato, M., Bedin, L. R., et al. 2018, ApJ, 853, 86
Bianchini, P., van de Ven, G., Norris, M. A., Schinnerer, E., & Varri, A. L. 2016, MNRAS, 458, 3644
Calamida, A., Strampelli, G., Rest, A., et al. 2017, AJ, 153, 175
Calamida, A., Zocchi, A., Bono, G., et al. 2020, ApJ, 891, 167
Cappellari, M., & Copin, Y. 2003, MNRAS, 342, 345
Clontz, C., Seth, A. C., Dotter, A., et al. 2024a, ApJ, 977, 14
Clontz, C., Seth, A. C., Wang, Z., et al. 2024b, arXiv:2412.09783
Dickson, N., Smith, P. J., Hénault-Brunet, V., Gieles, M., & Baumgardt, H. 2024, MNRAS, 529, 331
Dotter, A., Chaboyer, B., Jevremović, D., et al. 2007, AJ, 134, 376
Dotter, A., Chaboyer, B., Jevremović, D., et al. 2008, ApJS, 178, 89
Ferraro, F. R., Sollima, A., Pancino, E., et al. 2004, ApJL, 603, L81
Forbes, D. A. 2020, MNRAS, 493, 847
Foreman-Mackey, D., Conley, A., Meierjurgen Farr, W., et al. 2013a, emcee: The MCMC Hammer, Astrophysics Source Code Library, ascl:1303.002
Foreman-Mackey, D., Hogg, D. W., Lang, D., & Goodman, J. 2013b, PASP, 125, 306
Freeman, K. C., & Rodgers, A. W. 1975, ApJL, 201, L71
Gaia Collaboration, Weingrill, K., Mints, A., et al. 2023, A&A, 680, A35
Geyer, E. H., Hopp, U., & Nelles, B. 1983, A&A, 125, 359
Häberle, M., Neumayer, N., Bellini, A., et al. 2024a, ApJ, 970, 192
Häberle, M., Neumayer, N., Seth, A., et al. 2024b, Natur, 631, 285
Harris, C. R., Millman, K. J., van der Walt, S. J., et al. 2020, Natur, 585, 357
Hilker, M., Kayser, A., Richtler, T., & Willemsen, P. 2004, A&A, 422, L9
Hunter, J. D. 2007, CSE, 9, 90
Ibata, R. A., Bellazzini, M., Malhan, K., Martin, N., & Bianchini, P. 2019, NatAs, 3, 667
Johnson, C. I., & Pilachowski, C. A. 2010, ApJ, 722, 1373
Joo, S.-J., & Lee, Y.-W. 2013, ApJ, 762, 36
Kacharov, N., Alfaro-Cuello, M., Neumayer, N., et al. 2022, ApJ, 939, 118
Kamann, S., Husser, T. O., Dreizler, S., et al. 2018, MNRAS, 473, 5591
Lee, Y. W., Joo, J. M., Sohn, Y. J., et al. 1999, Natur, 402, 55
Libralato, M., Bellini, A., van der Marel, R. P., et al. 2018, ApJ, 861, 99
Libralato, M., Bellini, A., Vesperini, E., et al. 2022, ApJ, 934, 150
Limberg, G., Souza, S. O., Pérez-Villegas, A., et al. 2022, ApJ, 935, 109
Majewski, S. R., Nidever, D. L., Smith, V. V., et al. 2012, ApJL, 747, L37
Marino, A. F., Milone, A. P., Piotto, G., et al. 2011, ApJ, 731, 64
Massari, D., Koppelman, H. H., & Helmi, A. 2019, A&A, 630, L4
Mayor, M., Meylan, G., Udry, S., et al. 1997, AJ, 114, 1087
Merritt, D., Meylan, G., & Mayor, M. 1997, AJ, 114, 1074
Meylan, G., & Mayor, M. 1986, A&A, 166, 122
Milone, A. P., Piotto, G., Renzini, A., et al. 2017, MNRAS, 464, 3636
Myeong, G. C., Vasiliev, E., Iorio, G., Evans, N. W., & Belokurov, V. 2019, MNRAS, 488, 1235
Nitschai, M. S., Neumayer, N., Clontz, C., et al. 2023, ApJ, 958, 8
Nitschai, M. S., Neumayer, N., Häberle, M., et al. 2024, ApJ, 970, 152
Noyola, E., Gebhardt, K., & Bergmann, M. 2008, ApJ, 676, 1008
Noyola, E., Gebhardt, K., Kissler-Patig, M., et al. 2010, ApJL, 719, L60
Pagnini, G., Di Matteo, P., Haywood, M., et al. 2025, A&A, 693, A155
Pancino, E., Ferraro, F. R., Bellazzini, M., Piotto, G., & Zoccali, M. 2000, ApJL, 534, L83
Pancino, E., Seleznev, A., Ferraro, F. R., Bellazzini, M., & Piotto, G. 2003, MNRAS, 345, 683
Pavlík, V., Heggie, D. C., Varri, A. L., & Vesperini, E. 2024, A&A, 689, A313
Pavlík, V., & Vesperini, E. 2021, MNRAS, 504, L12
Pavlík, V., & Vesperini, E. 2022, MNRAS, 509, 3815
Pechetti, R., Kamann, S., Krajnović, D., et al. 2024, MNRAS, 528, 4941
Peebles, P. J. E. 1972, ApJ, 178, 371
Perez, F., & Granger, B. E. 2007, CSE, 9, 21
Pfeffer, J., Lardo, C., Bastian, N., Saracino, S., & Kamann, S. 2021, MNRAS, 500, 2514
Pryor, C., & Meylan, G. 1993, in ASP Conf. Ser. 50, Structure and Dynamics of Globular Clusters, ed. S. G. Djorgovski & G. Meylan (San Francisco, CA: ASP), 357
Reijns, R. A., Seitzer, P., Arnold, R., et al. 2006, A&A, 445, 503
Scalco, M., Bedin, L., & Vesperini, E. 2024, A&A, 688, A180
Sollima, A., Ferraro, F. R., Bellazzini, M., et al. 2007, ApJ, 654, 915
Soltis, J., Casertano, S., & Riess, A. G. 2021, ApJL, 908, L5
Spitzer, L. 1969, ApJL, 158, L139
Suntzeff, N. B., & Kraft, R. P. 1996, AJ, 111, 1913
Tailo, M., Di Criscienzo, M., D'Antona, F., Caloi, V., & Ventura, P. 2016, MNRAS, 457, 4525
Trenti, M., & van der Marel, R. 2013, MNRAS, 435, 3272
van de Ven, G., van den Bosch, R. C. E., Verolme, E. K., & de Zeeuw, P. T. 2006, A&A, 445, 513
van der Marel, R. P., & Anderson, J. 2010, ApJ, 710, 1063
van Leeuwen, F., Le Poole, R. S., Reijns, R. A., Freeman, K. C., & de Zeeuw, P. T. 2000, A&A, 360, 472
Vernekar, N., Lucatello, S., Kuzma, P., & Spina, L. 2025, arXiv:2502.17755
Villanova, S., Piotto, G., King, I. R., et al. 2007, ApJ, 663, 296
Villanova, S., Geisler, D., Gratton, R. G., & Cassisi, S. 2014, ApJ, 791, 107
Virtanen, P., Gommers, R., Oliphant, T. E., et al. 2020, NatMe, 17, 261
Watkins, L. L., van der Marel, R. P., Bellini, A., & Anderson, J. 2015a, ApJ, 803, 29
Watkins, L. L., van der Marel, R. P., Bellini, A., & Anderson, J. 2015b, ApJ, 812, 149
Watkins, L. L., van der Marel, R. P., Libralato, M., et al. 2022, ApJ, 936, 154
Weatherford, N. C., Chatterjee, S., Rodriguez, C. L., & Rasio, F. A. 2018, ApJ, 864, 13
Zocchi, A., Gieles, M., & Hénault-Brunet, V. 2017, MNRAS, 468, 4429
Zocchi, A., Gieles, M., & Hénault-Brunet, V. 2019, MNRAS, 482, 4713